

COSTA: the COLD Stream finder Algorithm.

Searching for kinematical substructures in the phase space of discrete tracers

M. Gatto^{1,4}, N.R. Napolitano^{2*}, C. Spiniello^{3,4}, G. Longo¹, and M. Paolillo¹

¹ University of Naples Federico II, C.U. Monte SantAngelo, Via Cinthia, 80126, Naples, Italy

² School of Physics and Astronomy, Sun Yat-sen University Zhuhai Campus, 2 Daxue Road, Tangjia, Zhuhai, Guangdong 519082, P.R. China

³ Sub-Department of Astrophysics, Department of Physics, University of Oxford, Denys Wilkinson Building, Keble Road, Oxford OX1 3RH, UK

⁴ INAF-Osservatorio Astronomico di Capodimonte, Via Moiariello 16, 80131, Naples, Italy.

Received 24 July 2020

ABSTRACT

Context. We present COSTA (COLD Stream finder Algorithm), a novel algorithm to search for cold kinematical substructures in the phase space of planetary nebulae (PNe) and globular clusters (GCs) in the halo of massive galaxies and intracluster regions.

Aims. COSTA aims at detecting small sized, low velocity dispersion streams, as the ones produced in recent interactions of dwarf galaxies with the halo of more massive galaxies, including the ones sitting in the central region of rich galaxy clusters.

Methods. COSTA is based on a deep friend-of-friend procedure that isolates groups of N particles with small velocity dispersion (between 10 km s^{-1} and $\sim 100 \text{ km s}^{-1}$), using an iterative (n) sigma-clipping over a defined number of (k) neighbor particles. The algorithm has three parameters ($k - n - N$), plus a velocity dispersion cut-off, which defines the “coldness” of the stream, that are set using Montecarlo realizations of the sample under exam.

Results. In this paper, we show the ability of COSTA to recover simulated streams on mock data-sets of discrete kinematical tracers with different sizes and measurement errors, from publicly available hydrodynamical simulations. We also show the best algorithm set-up for a realistic case of stream finding in the core of the Fornax cluster, for future applications of COSTA to real populations of PNe and GCs.

Conclusions. COSTA can be generalized to all problems of finding small substructures in the phase space of a limited sample of discrete tracers, provided that the algorithm is trained on realistic mock observations reproducing the specific dataset under exam.

Key words. XXX - XXX - XXX

1. Introduction

In the hierarchical formation scenario, massive structures grow in a bottom-up manner assembling mass by merging of small systems (White & Rees 1978). This is a process that is still ongoing, as demonstrated by cosmological simulations (Naab et al. 2007, 2009; Cooper et al. 2010; Oser et al. 2010, 2012).

In the Local Group, the accretion of smaller building blocks has been observed in the last decades (Ibata et al. 1994, 1995; Yanny et al. 2000) under the form of dwarf debris (Ibata et al. 2001b; Majewski et al. 2003). In denser environments, like galaxy groups or clusters, this mechanism is enhanced because of the whirl of encounters and collisions, leading to the formation of an extended halo around the central galaxy (e.g. Cooper et al. 2010). Central dominant (cD) galaxies in the innermost region of the richest clusters are the archetypes of this scenario, with their exceptional merging histories (e.g. Ruszkowski & Springel 2009; Weinzirl et al. 2014; Iodice et al. 2016). The remarkable large stellar masses of cDs ($M_{\star} \geq 10^{12} M_{\odot}$) are well explained in the hierarchical scenario, as the mass assembly is expected to happen either through tidal stripping of stars

and globular clusters from their satellite or dwarfs (Gallagher & Ostriker 1972; Moore et al. 1996; Gregg 1998; Willman et al. 2004; Read et al. 2006), or through major mergers with other bright galaxies or minor ones in which the cD ‘eats’ smaller systems (Ostriker & Tremaine 1975; White 1976; Malumuth & Richstone 1984; Merritt 1985; Liu et al. 2015; Nipoti 2017). In particular, numerical simulations and semi-analytic models have demonstrated that the bulk of their accreted mass and extended halos was built up in the last few Gyr, especially through minor merger events (e.g. De Lucia & Blaizot 2007; Amorisco 2019). As all these processes are expected to be still in action, one can search for observational signatures of such events in the cluster core, either with the deep photometry (see e.g. Mihos et al. 2005; Iodice et al. 2017; Mihos et al. 2017) or in the kinematics of stars and other kinematical tracers as planetary nebulae and globular clusters (e.g. Napolitano et al. 2003; Romanowsky et al. 2012; Longobardi et al. 2015; Spiniello et al. 2018; Pota et al. 2018; Amorisco 2019). Hence, stellar substructures in galaxy haloes (and beyond, i.e. in the intracluster regions), under the form of debris of past or recent merger events, are invaluable pieces of information to study the mechanisms supplying mass in the assembly history of galaxies in dense environments.

* E-mail: napolitano@mail.sysu.edu.cn

In recent years, the study of the signature of minor mergers in the local universe, like halo shells and ripples, tidal streams or other stellar substructures, has become an important tool to probe the assembly histories of galaxies (e.g. [Helmi et al. 1999](#); [Ibata et al. 2001a](#); [Belokurov et al. 2006](#); [Tal et al. 2009](#); [Martínez-Delgado et al. 2010](#); [Cooper et al. 2011](#); [Mouhcine et al. 2011](#); [Xue et al. 2011](#); [Bate et al. 2014](#)). The number of newly discovered stellar streams and other substructures in the halos of nearby galaxies has dramatically increased, showing that remnants of merger events could be almost ubiquitous. Among the most important examples, we can count the Sagittarius Stream in the Milky Way ([Ibata et al. 1997, 2001c](#); [Majewski et al. 2003](#)) and many other substructures detected around M31 (Andromeda galaxy; e.g. [McConnachie et al. 2009](#); [Ibata et al. 2001d](#)).

Early investigations of such substructures were based on photometric observations. However, this approach is challenging due to the faint surface brightness of the remnants, typically below $\mu \sim 27$ mag/arcsec². This implies that only the brightest substructures are generally detected, while most of the accreted mass provided by the fainter events, having generally a surface brightness of the order of 30 mag/arcsec² or below ([Cooper et al. 2010](#)), remain hidden in the central galaxy background.

In the last few years, deeper and more accurate spectroscopy has allowed to include kinematic information of the debris, in order to go beyond the purely photometric studies and look into the phase-space (projected positions and line-of-sight velocities) to search for the typical signatures expected in these interactions (e.g. [Johnston et al. 2008](#); [Romanowsky et al. 2012](#)). Within the Local Group, these substructures can be studied using individual stars (e.g. [Koch et al. 2008](#); [Gilbert & Vacca 2009](#); [Starkenburger et al. 2009](#); [Xue et al. 2011](#); [Belokurov & Koposov 2016](#)). Outside the Local Group stars cannot be resolved and other kinematic tracers have to be used. Planetary nebulae (PNe) and globular clusters (GCs) are suitable tracers of this kind as they are observable out to large distances from the galaxy centers ([Durrell et al. 2003](#); [Merrett et al. 2003](#); [Douglas et al. 2007](#); [Shih & Méndez 2010](#); [Cortesi et al. 2011](#); [Richtler et al. 2011](#)) and their velocity can be measured with good precision in nearby galaxies and galaxy clusters. They represent a viable alternative to study the outskirts of galaxies where it is very hard to measure stellar absorption lines and thus obtain kinematical information from the integrated light (PNe: [Hui et al. 1995](#); [Napolitano et al. 2002](#); [Romanowsky et al. 2003](#); [De Lorenzi et al. 2009](#); [Coccatto et al. 2009](#); [Napolitano et al. 2009](#); [Richtler et al. 2011](#); [Forbes et al. 2011](#); [Pota et al. 2013](#); [Longobardi et al. 2015](#); [Hartke et al. 2017](#); [Spiniello et al. 2018](#); GCs: [Côté et al. 2003](#); [Romanowsky et al. 2009](#); [Schuberth et al. 2010](#); [Woodley & Harris 2011](#); [Romanowsky et al. 2012](#); [Foster et al. 2014](#); [Veljanoski & Helmi 2016](#); [Pota et al. 2018](#); [Longobardi et al. 2018](#)).

The combined information of position and velocity of tracers in the halo regions of galaxies allows us to study substructures in the tracer phase-space, where they have not yet fully mixed due to the long dynamical times ([Napolitano et al. 2003](#); [Arnaboldi et al. 2004](#); [Bullock & Johnston 2005](#); [Arnaboldi et al. 2012](#); [Coccatto et al. 2013](#); [Longobardi et al. 2015](#)).

Historically, the methods adopted to search for streams have been very empirical and lacking well encoded (objective) criteria to systematize the search of streams in the full phase-space. Only recently, there has been a large effort to develop stream finding algorithms suitable for different data sets. For the Milky Way, [Malhan & Ibata \(2018\)](#), implemented STREAMFINDER, with the aim of unveil dynamically cold structures in the 6D phase-space, by taking advantage of the Gaia space mission data. This

code looks for a handful number of particles (as few as 15 members) which lie along a similar orbit, allowing to detect tiny and ultra-faint streams in the Galactic Halo. Other algorithms have been focused on automatic search of tidal structures, like shells or ridges, in deep images (e.g. [Kado-Fong et al. 2018](#); [Hendel et al. 2019](#)). Such approaches are more directed to large sample of galaxies to build statistically significant samples of stream features, but they do not rely on kinematics. As stated before, this is not ideal to look for low-surface brightness tidal features, as expected to be those originating from minor mergers (see [Cooper et al. 2010](#)).

In this context, we present COSTA, the COLD STREAM finder Algorithm, a new method to search for candidate cold substructures which can be interpreted as signatures of recent or past interaction between a main galaxy and the dwarf galaxies surrounding it. COSTA aims to fill the gap, left by the above algorithms, introducing a method that relies on kinematics (namely a reduced 3D phase-space of projected positions and line-of-sight velocities) which can reveal streams even beyond the Local Group and that can be still applied to large galaxy samples but below the detection limits imposed by the photometry.

We introduce the basic statistical methods that allow the identification of cold kinematical substructures made of few tens of particles, compatible with what is expected for faint streams around galaxies. The method is based on a k-nearest-neighbors approach (KNN), which groups nearby particle in 2D positions and in velocity to find coherent kinematic substructures.

The algorithm is general and can be applied to any nearby stellar system, either galaxies or galaxy clusters cores (where large galaxy haloes and intracluster light concentration reside).

As a template case of this latter kind to show the potential of the method, we discuss here the specific case of the Fornax cluster core. The Fornax cluster is particular suitable for such a test as different studies have provided evidences of recent galaxy interactions (e.g. [D'Abrusco et al. 2016](#); [Iodice et al. 2017](#); [Spiniello et al. 2018](#); [Sheardown et al. 2018](#)). This complexity represents a challenging test bench for the algorithm.

Here, in this paper, we use mock observation of the Fornax Cluster to assess the reliability of the method and to demonstrate how to set-up the best parameters in a real case. In a companion paper (in preparation), we will then apply COSTA to identify real streams of GCs and PNe from the Fornax VST Spectroscopic Survey (FVSS, [Pota et al. 2018](#); [Spiniello et al. 2018](#), hereafter P+18 and S+18 respectively).

The paper is structured as follows: in Section §2 we present a brief description of the algorithm. In Sections §3 and §4 we test it on hydrodynamical simulations of pair interacting galaxies and on Montecarlo simulations of the Fornax cluster core, respectively. Finally, in Section §5 we draw our conclusions.

2. COSTA: The COLD STREAM finder Algorithm

In this section we introduce the COLD STREAM finder Algorithm (COSTA) to detect cold substructures in the reduced phase space (position on the sky and radial velocity) of discrete tracers.

In order to find cold substructures that are correlated both in position and in velocity, we implemented an algorithm looking for points close both in the RA/DEC position-space and in the reduced phase-space (velocity vs. radius). The method relies on a pseudo-KNN method which is based on a deep *friend-of-friend* algorithm that isolates groups of (N) particles with a small velocity dispersion (σ_{cut} , chosen between 10 km s⁻¹ and ~ 100 km s⁻¹).

Table 1. Parameters of the selected galaxies in the galmer simulation. The values of the velocity dispersion σ_v , listed in the last column, have been measured in the configuration $N_{\text{giant}} = 2000 - N_{\text{dwarf}} = 150$

	M_B [$2.3 \times 10^9 M_\odot$]	M_H [$2.3 \times 10^9 M_\odot$]	M_{disk} [$2.3 \times 10^9 M_\odot$]	r_B [Kpc]	r_H [Kpc]	N_{stars}	N_{DM}	N_{gas}	σ_v [kms^{-1}]
gE0	70	30	0	4	7	320000	160000	0	145
dE0	7	3	0	1.3	2.2	32000	16000	0	77
gSa	10	50	40	2	10	240000	160000	80000	162
dS0	1	5	4	0.6	3.2	32000	16000	0	149

The main difficulty is to efficiently detect particles belonging to the stream, which should preserve the low velocity dispersion of the dwarf progenitor while they are moving in regions where the potential of the cluster rules and the local velocity dispersion is the one of the cluster (i.e. up to 50 times larger than typical dwarf-like velocity dispersions). To do that, for each particle, the algorithm starts performing an iterated sigma clipping on a number (k) of neighbors. In particular, it removes all the particles with a velocity outside the interval $[\bar{v} - n \times \sigma, \bar{v} + n \times \sigma]$, where \bar{v} and σ are the mean velocity and the velocity dispersion of the k particles and n is the sigma clipping value. As a proxy for the velocity dispersion, we use the standard deviation of the individual velocities (see §3.2). The algorithm iterates the procedure, with the mean velocity and velocity dispersion of the remaining particles, until there are no outliers to be clipped. Once the procedure is over, the algorithm selects all structures in the position and velocity space with a minimal number (N_{min}) of particles.

To define the maximum velocity dispersion acceptable for a given substructure to be considered cold, COSTA uses another parameter, the cut-off velocity dispersion, σ_{cut} . We fine-tune our algorithm to find cold streams originating from the interaction of dwarf galaxies with the cluster. In fact, we expect that dwarf disruption is the main mechanism contributing to the later formed intracluster stellar population and the assembly of large stellar halos around galaxies. Hence, we allow for σ_{cut} values ranging from 10 to $\sim 100 \text{ kms}^{-1}$, based on the typical dwarf-like dispersion values found in the Coma cluster (Kourkchi et al. 2012).

The final COSTA output is then a list of substructures with low velocity dispersion, below the fixed threshold, σ_{cut} .

We note here that more massive galaxies would produce more diffuse substructures, due to a higher velocity dispersion and larger sizes. These would be harder to be “filtered” in the phase space as they would be more mixed to the warm halo environment.

Thus, to summarize, the COSTA algorithm has, in total, three parameters (k , n , N_{min} for any given (upper) dispersion threshold, σ_{cut} , that need to be properly chosen to maximize the number of real cold substructures (completeness) and minimize the number of spurious detections (purity), caused by the intrinsic stochastic nature of the velocity field of hot systems. To this purpose, one can use Montecarlo realizations of the specific sample under exam.

Our approach has the advantage of being able to refine the selection of coherent spatial and velocity substructures, but it has the disadvantage to be biased toward round geometries. In fact, the algorithm is based on a simple metric which uses the distances from every single particle. This reduces the chance to identify chain-like structures, which are likely expected in elongated streams. To remove this bias, we add a second stage in COSTA, where we verify if some of the groups do belong to a single structure. In particular, we define two or more groups belonging to a single structure if they show at least one common

particle and their velocity dispersion values differ by less than their uncertainties.

To demonstrate that it is possible to identify regions in this parameter space that can reliably detect streams with an acceptable fraction of false positives, we first test the algorithm over a simulated sample from the publicly available hydrodynamical simulations Galmer (Chilingarian et al. 2010), and then train the algorithm to search for stellar streams in the Fornax cluster core. The results of these tests are presented in the next Sections.

3. Testing COSTA on hydrodynamical simulations

We use a suite of publicly available simulations, the Galmer database (Chilingarian et al. 2010), to test the ability of our algorithm to recover streams originating from a dwarf during a close passage to a giant galaxy. The simulated data-cubes are needed to test the algorithm self-consistently.

We first define the series of (k , n , N_{min} , σ_{cut}) set-ups that minimize the false detections, and then apply them to find the stream. Finally, we check how meaningful the recovered properties (e.g. mean velocity, local velocity dispersion, fraction of particles) are with respect to the intrinsic property of the stream. At this point, we are interested to verify whether for a given stream there is a series of parameter set-ups that allow COSTA to find it and how these might change as a function of the observational conditions (i.e. measurement errors and total number of particles).

3.1. The Galmer Simulations

The Galmer simulations are based on a Tree-Smoothed Particle Hydrodynamics (SPH) code, in which gravitational forces are calculated using a hierarchical tree method (Barnes & Hut 1986) and gas evolution is followed by means of SPH (Lucy 1977; Gingold & Monaghan 1982). Dark matter particles and baryon particles have both masses of $\sim 10^5 M_\odot$, while the softening lengths is $\epsilon = 280 \text{ pc}$ for giant-giant interactions, and $\epsilon = 200 \text{ pc}$ for giant-intermediate and giant-dwarf runs. This gives an appropriate mass and spatial resolution to trace low mass and low surface brightness substructures. The typical mass residing in stellar streams stripped by the dwarf during his interaction with the large galaxy is of the order of 10% of its mass, i.e. given the typical GC and PN specific number densities (the number of particle per unit of luminosity) the stream is fairly sampled with a few tens and up to hundred tracers (e.g. GCs and PNe together). We will simulate different depth of our observational set-up by assuming different numbers of stellar particles expected to populate the stream.

The advantage of testing the algorithm on simulations is that we can separate the particles belonging to the dwarf galaxy from the ones belonging to the target system. We can, therefore, characterize the phase-space of both galaxy target and streams produced in the fly-by of the dwarf galaxy through the central galaxy halo.

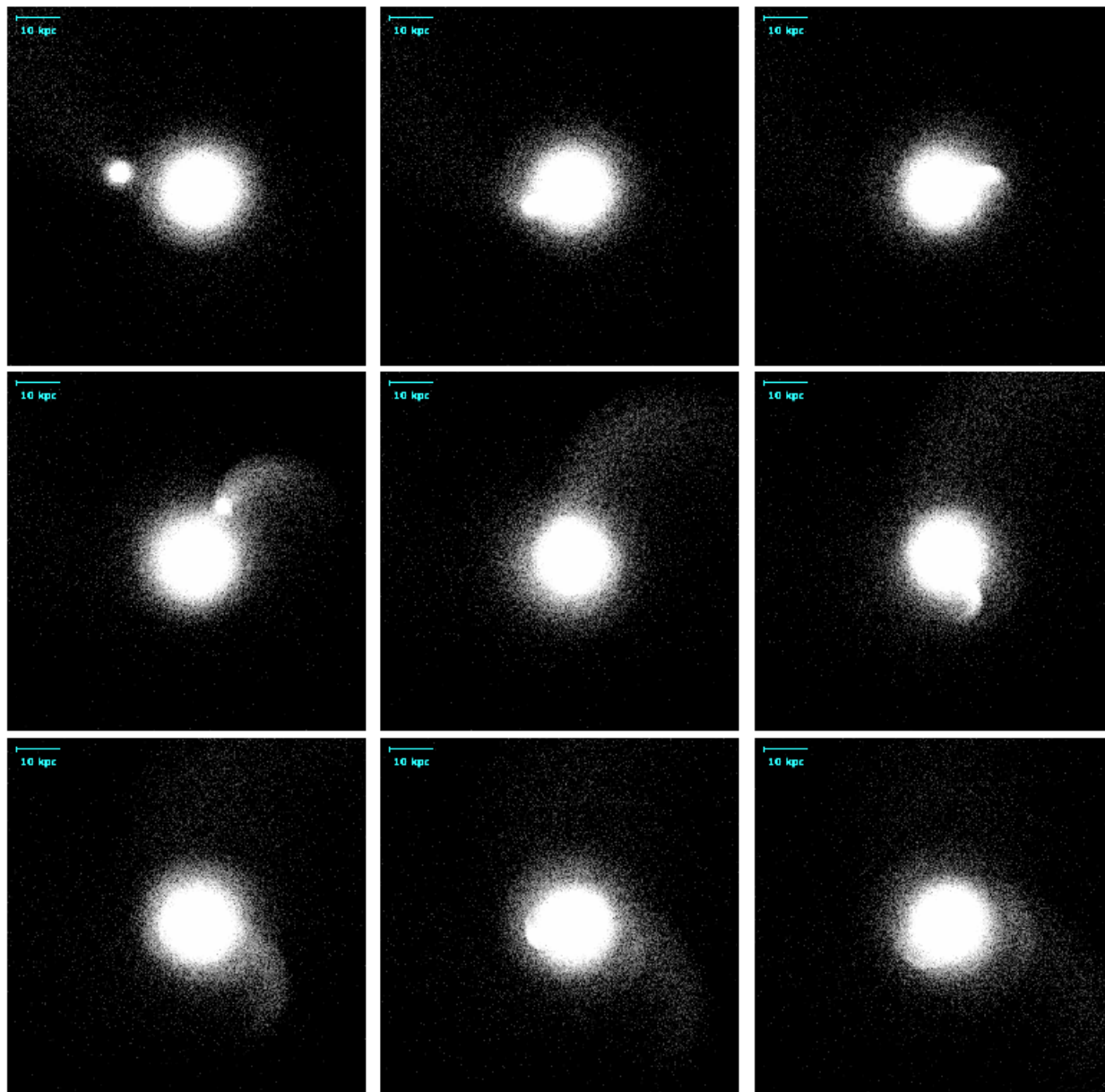


Fig. 1. Snapshots of the gE0-dE0 encounter, from 1850 Myr (top left) up to 2250 Myr (bottom right) after the begin of the simulation, and separated by steps of 50 Myr. To test COSTA, we use the configuration at the center of the image, temporarily located at 2050 Myr after the start of the encounter.

The Galmer database¹ provides about 1019 simulations of colliding galaxies and more than 70000 snapshots showing the development of these interactions up to 3 Gyr from the beginning of the encounter with a bin interval, for each snapshot, of 50 Myr.

From the whole database, we focus on two encounter configurations: 1) the one between a giant Elliptical galaxy, gE0, and a dwarf E0 galaxy, dE0, with a mass ratio of 1:10 (the minimum found in the database for all simulations) and 2) the one between a giant Sa galaxy, gSa, and a dwarf S0, dS0, galaxy, also with a mass ratio 1:10. Table 1 shows the parameters of the four galaxies. We need to point-out that a mass ratio of 1:10 is not optimal to generalize the results, as a wider population of systems, also with lower mass ratio, exist in real cases. As we will show later, though, this is a conservative starting point as our algorithm is

more efficient in detecting group in phase-space which are generally much colder than the surrounding environment. Hence, the difference in velocity dispersion which characterize the Galmer systems are representative of extreme cases: if COSTA is able to detect substructures in these systems, then it will be even more successful in cases involving lower mass satellites.

We select the gE0-dE0 and gSa-dS0 cases as realistic representations of the dynamics of a dwarf-giant encounters. In particular the case of the gE0-dE0 is fairly representative of a typical encounter between a hot, high dispersion system and a colder satellite, like the one happening in large galactic halos (see e.g. Cooper et al. 2010; Iodice et al. 2016). In both configurations, we choose an encounter with the satellite starting 100 kpc away, and falling toward the larger galaxy in a prograde orbit with an inclination of 33 degrees and a pericentral distance of 16 kpc. We initially used a prograde orbit because this is expected to ex-

¹ <http://galmer.obspm.fr>

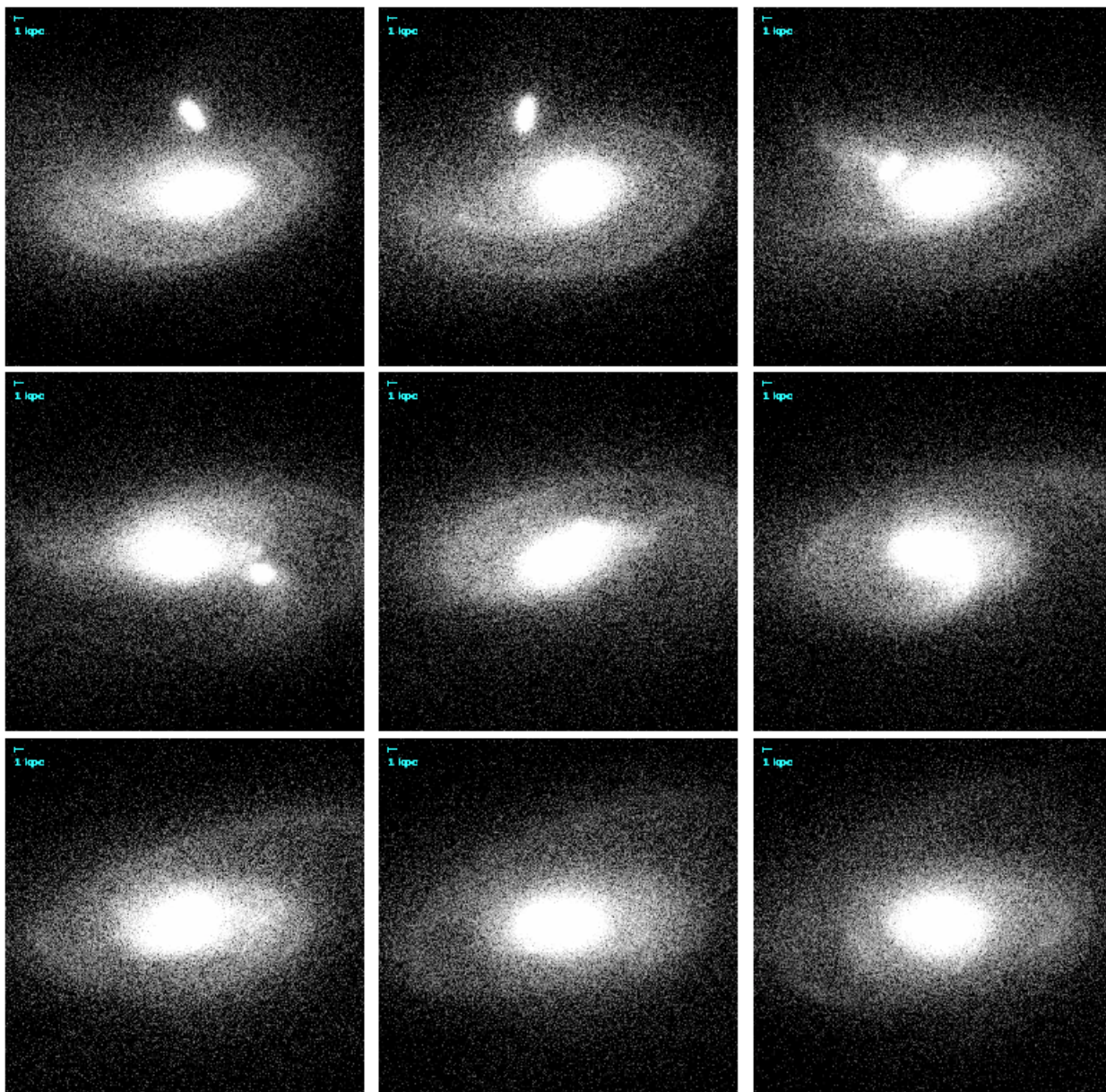


Fig. 2. Same as Fig. 1 but in the case of the gSa-dS0 interaction. These snapshots correspond to a time interval comprised between 1650 Myr and 2050 Myr after the begin of the simulation, with our test configuration (1850 Myr) at the center of the image.

change a lower amount of energy and therefore to minimize the scatter of dwarf particles into warmer tails. However, since in the case of the gSa-dS0 encounter the dwarf and the giant stars were too mixed, for this latter case we also consider a retrograde encounter.

In Fig. 1 and Fig. 2, we show a few snapshots of the gE0-dE0 and gSa-dS0 encounters, respectively. The final configuration we adopt for our tests is shown in the central panel (encounter), while the other panels show different time-snaps, each one spaced in time by 50 Myr, with the top left corner temporarily located 200 Myr before the chosen configuration. The choice of the central configurations is motivated by the fact that there the distance between the intruder and the giant galaxy is the shortest (as evident also from figures 1 and 2). This allows us to have a sufficient spatial mix of the two systems, and thus stress as much as possible the ability of COSTA to recover stream particles well embedded in high density regions.

From the figures, it is also clear that the encounters start producing a stream-like structure since the first passage at a few tens of kpc. Particles belonging to the original stream become mixed after a few hundreds Myr, but subsequent close passages produce even brighter streams. These latter remain visible and well separated from the background galaxy for hundreds of Myr. Then, later on in time, they diffuse and mix with galaxy halo particles. This time scale is set by the specific dynamical time of the system under exam and, for hotter central systems and lower mass ratios, this can be larger. Unfortunately, the Galmer database does not provide lower mass ratios than the ones adopted here. Nevertheless, these examples allow us to test the ability of COSTA in finding such cold streams as a function of a few observational parameters.

3.2. Running COSTA on Galmer simulations

In order to apply COSTA to Galmer simulations, we first need to extract from the simulated 6D datacubes a velocity field (i.e. RA and DEC, and a radial velocity) that mimics a typical observational situation. Then, COSTA can be applied to the mock velocity field to recover the cold substructures, together with their intrinsic kinematical parameters. Here, we intend to test the capability of identifying streams made of a few particles in velocity fields of different sizes. In particular we test the case of $N_{\text{part}} = 2000, 1000, 500$ extracted from the giant galaxy. These are typical number of test particles found in external galaxies, like planetary nebulae (Fornax cluster: $\sim 1000, \sim 1500$ PNe: Spiniello et al. 2018 and references therein; M31, ~ 2000 PNe: Merrett et al. 2006; NGC 5128, ~ 1100 PNe: Peng et al. 2004; NGC 4374, ~ 500 PNe: Napolitano et al. 2011) or globular clusters (Fornax cluster: ~ 1000 GCs: Pota et al. 2018 and references therein; M87, ~ 500 : Romanowsky et al. 2012). For the dwarfs, we consider instead $N_{\text{part}} = 150, 75, 38$, respectively (e.g. Fahrian et al. 2020). These number of particles are chosen to match with the expected particles observable from streams of surface brightness of the order of 28-30 mag arcsec⁻² (see discussion below).

Finally, to test different observational conditions, we adopt, for each of the three different selected encounters (i.e. gE0-dE0 and gSa-dS0 prograde/retrograde), three orders of measurement errors, $\Delta_v = 10, 20, 40$ km s⁻¹ by re-sampling the particle velocities with a Gaussian distribution centered on the particle velocity and having $\sigma = \Delta_v$ (v_{obs} hereafter). These values are comparable to what typically reached with mid and low spectral resolution. Measurement errors have the effect to dilute the observed velocity distribution of the cold substructure by increasing the observed squared velocity dispersion, i.e. $\sigma_{\text{obs}}^2 = \sigma_I^2 + \Delta_v^2$, where we indicate with σ_I the intrinsic velocity dispersion of the stream and with σ_{obs} the observed velocity dispersion.

In the following, we define the mean velocity and velocity dispersion of the detected substructures using some standard statistical definition (see also P+18):

$$v_{\text{mean}} = \frac{1}{N} \sum v_{\text{obs},i}, \quad \sigma_I^2 = \frac{1}{N-1} \sum (v_{\text{obs},i} - v_{\text{mean}})^2 - (\Delta_v)^2. \quad (1)$$

Hence, the larger the Δ_v is, the larger the chance is that a cold structure become warm enough to skip the cold criterion on σ_{cut} , or that some of the particles are discarded by the sigma-clipping part of the algorithm. This would then leave too few particles to meet the minimum particle number (N_{min}) limit, hence making COSTA losing good candidate streams.

3.3. Setting the reliability of COSTA

Before running COSTA to search for streams, we need to check whether and how often COSTA returns spurious detections. In the case of simulations, this is easily performed by running COSTA on the central galaxy particles only, which represents the smooth warm background, over which streams have to be found when the intruder is added.

For our analysis, we define the following datasets:

- *white noise sample (WNS)*: RA, DEC and v_{obs} of the giant galaxy or cluster regions without any artificial stream added;
- *detection sample (DS)*: RA, DEC and v_{obs} of the full system including the WNS and the particles of the stream.

We use the WNS to select those set-ups (i.e. combination of k, n, N_{min} and σ_{cut}) that have a reasonably low probability to find artificial detection and to be used to look for streams in the DS. A given set-up that finds no spurious in the WNS has maximum “reliability”, which means that if it detects a stream in the DS then this is likely to be real. On the other hand, a set-up that finds many spurious detections is highly unreliable and has to be discarded.

In order to have a statistical definition of the reliability of the set-ups in the k, n, N_{min} and σ_{cut} space, we use 100 different mock datasets randomly extracted from all particles in the simulations. We use different combinations of number of particles N_{part} and velocity errors Δ_v for each of the three encounters, and present here some representative cases. Specifically, we discuss the cases where we randomly extract 2000 particles with errors $\Delta_v = 10$ and 40 km s⁻¹; 1000 particles with $\Delta_v = 40$ and 500 particles with $\Delta_v = 20$ km s⁻¹. For each case, we uniformly sample the k, n, N_{min} parameters space, for different σ_{cut} and run COSTA with all the possible combinations of the free parameters selected in the following ranges:

- k : from 10 to 30 with steps of 5
- n : from 1.3 to 3 with steps of 0.2-0.3
- N_{min} : all values from 5 up to k
- σ_{cut} : from 10 to 80 km s⁻¹ with steps of 5 km s⁻¹

For each combination of these parameters we define the reliability over the 100 random extractions as

$$\text{Rel} = 100 - N_{\text{spu}} \% \quad (2)$$

where N_{spu} is the number of times we obtain at least one spurious detection from COSTA.

We use 70% as threshold to define a set-up reliable. This threshold is somehow arbitrary, as it might depend on the risk one is willing to take in considering a group of particles as a stream. In principle, one should set the reliability toward 100%, to be sure that none of the detection is spurious. However, this could result in a too conservative choice that might cut all streams that are statistically closer to the white noise given by the background particles. For instance, the properties of streams with a small number of particles and/or too close to the σ_{cut} may be very close to the properties of the spurious detections, and thus would be filtered out by too conservative thresholds. For this reason we are motivated to choose a lower threshold which might provide a larger completeness but a lower purity, due to the increased chance to find some spurious detections. Since the main scope of COSTA is to provide stream candidates that shall be confirmed with deeper observations, then a fair amount of false detections are acceptable. We will discuss the impact of the threshold in §3.6.

Here below we discuss the results for the gE0-dE0 and the gSa-dS0 encounters separately and in details.

3.4. The case of gE0-dE0 encounter

We first test COSTA parameter combinations on the WNS to check which configurations produce spurious detections over 100 re-extractions of the same catalog, re-sampling the velocity errors for each particle. We exclude the particles in the central 1 kpc of the main galaxy, since these regions are usually highly incomplete in discrete tracers’ detection (see e.g. Napolitano et al. 2001) and any attempt to look for streams would produce very uncertain results.

Then, we collect all configurations which return at least 70% of the re-simulated field COSTA analysis with no spurious detection (e.g. $\text{Rel} \geq 70$).

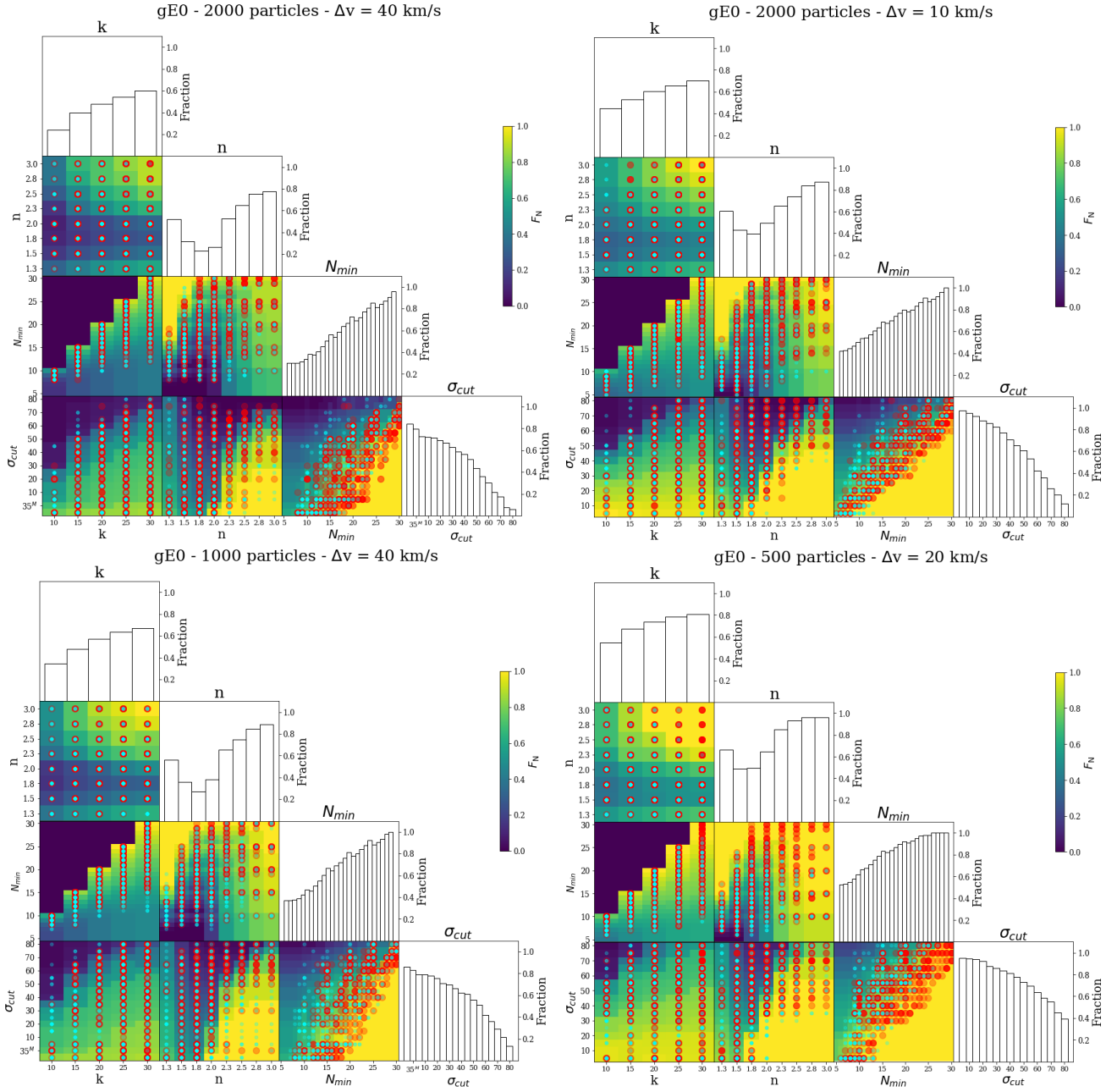


Fig. 3. Scatter plot between all the possible free parameter pairs, color-coded by the fraction of times (F_N) a given couple of parameters has a reliability greater than 70% over the total number of possible configurations, along with the distribution of each parameter. Red points (cyan points) indicate the combination of parameters where COSTA detected a real (spurious) stream in ten random extraction of the giant+dwarf system.

3.4.1. Reliability as a function of the COSTA parameters

In Fig. 3 we show, for the four different combinations of $N_{\text{part}} - \Delta v$, the scatter plot between all the possible free parameter pairs, color-coded by the fraction of times a given pair overcomes the chosen threshold on the reliability, marginalized over the other two free parameters. This cumulative fraction, related to each parameter pair, is hence defined as

$$F_N = \frac{\# \text{ parameter-pair with Rel. } \geq 70\%}{\# \text{ total tests for a fixed parameter-pair}}$$

The latter quantity is expected to be higher for the combinations of parameters that have a lower chance to produce spurious detection for any other choice of the other parameters, and,

as such, it represents a quality flag for a given configuration. Indeed, when a parameter configuration with a low F_N finds a stream, the chance that this is a spurious one is higher. In the following, we will use the high F_N regions in the parameter space to label the detection as higher-quality (see also below), as they represent the regions where all parameters give a high reliability.

In Fig. 3 the regions of the parameter space that reach the maximum level of reliability ($> 70\%$ for all possible parameter configurations) are shown in yellow, while the quality of the configuration degrades toward the blue as the fraction of $>70\%$ reliability decreases over the total combination including that particular pair. For the yellow area, this means that, having fixed two of the four free parameters, the threshold for the reliability is reached regardless the values of the other two.

Looking at the results for the different $N_{\text{part}} - \Delta_v$ cases, we can see that regions with $F_N \sim 1$ are located at the upper right corner of the $k - n$, on the diagonal of the $k - N_{\text{min}}$, at the bottom right corner of the $k - \sigma_{\text{cut}}$, $n - \sigma_{\text{cut}}$ and of the

$$N_{\text{min}} - \sigma_{\text{cut}}$$

panels, at the upper left corner and right side of the $n - N_{\text{min}}$ projection. This is valid for all $N_{\text{part}} - \Delta_v$, but with different extensions. Moreover, many other regions in the parameter space have a $F_N > 70\%$ (light green color), indicating that there are numerous combinations of the four parameters yielding a high reliability, and hence producing very reliable streams with little or no chance to be spurious.

The same figure also shows the one dimensional distribution of all the four COSTA parameters, corresponding to $\text{Re}l > 70\%$, showing which are the peak values in the parameter space that allow the largest chance of producing little or no spurious streams.

In particular, the distribution of N_{min} shows that this is a critical parameter to avoid spurious detections, as the probability of finding spurious structures (i.e. groups of particles with similar velocities) is larger for small N_{min} and monotonically decreases as N_{min} increases, producing a higher overall reliability at larger N_{min} . Indeed, too small N_{min} would increase the chance that a bunch of particles in k neighbors have close velocities by chances, thus returning a spurious detection. On the other hand, as N_{min} defines the minimal mass of the stream that COSTA would detect, too large N_{min} will produce high reliability but also high incompleteness in the final list of stream candidates (as small streams would be filtered out).

The distribution of σ_{cut} , instead, justifies our choice to avail with many cut-offs, as larger values allow us to find warmer streams with larger N_{min} (F_N is close to 1 in the bottom right of the $N_{\text{min}} - \sigma_{\text{cut}}$ panel), while lower σ_{cut} minimize the number of spurious structures (from the 1D distribution of the σ_{cut} Fraction). About the σ_{cut} parameter, it is worth mentioning that we adopt cut-offs in some case lower than the nominal instrumental errors. This is because a stream with an intrinsic velocity dispersion smaller than the instrumental error would give an observed value which can be any random number smaller than Δ_v . Hence, using $\sigma_{\text{cut}} \geq \Delta_v$ would exclude real stream colder than Δ_v . Using smaller cuts, we expect to detect such streams, although we cannot evaluate their intrinsic kinematics. In this cases, we will consider the $\sigma_{\text{mea}} \sim \sigma_{\text{obs}}$, i.e. without subtracting Δ_v in quadrature, and mark this latter with an apex.

Looking at the n distribution, the set-ups with the highest reliability fractions are located at high n , since a shallow sigma-clipping remove less outliers. Hence only structures with an initial low velocity dispersion value fall below a given threshold, unless one sets a higher N_{min} , in which case there is little chance of finding a spurious structure with small n (see e.g. the central panel in the top left of Fig. 3).

Finally, the k distribution increases monotonically. Since the higher is k the larger are the possible values of N_{min} (N_{min} is varied from 5 up to k), it is expected that this distribution mimics the trend of the N_{min} one.

As all the previous considerations may be dataset dependent, it is crucial to explore the behavior of the reliability in the parameter space as a function of the number of particles, the velocity errors and also the minimal reliability threshold (e.g. changing this to a lower or higher threshold than 70%). In this section we take care of the first two quantities (number of particles and the velocity errors), while we will discuss the reliability threshold in §3.6.

Table 2. *Column 1:* adopted configuration. *Column 2:* percentage of set-ups where the stream has been recovered with respect to the total set-ups in which COSTA detected at least a cold substructure averaged on ten simulations. *Column 3:* the contaminant fraction (CF, see definition in the text).

gE0 - dE0	F_N	CF
2000 part - 40 km s ⁻¹	0.54 ± 0.18	0.71 ± 0.12
^a 2000 part - 40 km s ⁻¹	0.59 ± 0.24	0.73 ± 0.11
2000 part - 10 km s ⁻¹	0.54 ± 0.08	0.67 ± 0.13
^a 2000 part - 10 km s ⁻¹	0.67 ± 0.10	0.71 ± 0.12
1000 part - 40 km s ⁻¹	0.40 ± 0.22	0.70 ± 0.13
^a 1000 part - 40 km s ⁻¹	0.47 ± 0.25	0.71 ± 0.12
500 part - 20 km s ⁻¹	0.51 ± 0.20	0.64 ± 0.17
^a 500 part - 20 km s ⁻¹	0.56 ± 0.21	0.66 ± 0.17

a: in these configurations we ruled out set-ups with $F_N < 50\%$ in the $n - N_{\text{min}}$ space as described in the text.

By comparing Fig. 3 top-right panel, which shows the case of a lower $\Delta_v = 10 \text{ km s}^{-1}$ with the top-left panel, showing $\Delta_v = 40 \text{ km s}^{-1}$ the number of possible combinations which have $\text{Re}l \geq 70\%$ increases by more than 10% when considering smaller errors. In fact, the smaller velocity error values allow COSTA to recognize more efficiently the absence of streams without spurious detections. This is quite encouraging, as it shows that there is little room for spurious cold structures to be produced by the white noise of the background velocity field. Also, this shows that the velocity measurements are crucial to increase the purity of stream detection.

The bottom left and right panels of Fig. 3 show the configurations with 1000 and 500 particles with $\Delta_v = 40 \text{ km s}^{-1}$ and $\Delta_v = 20 \text{ km s}^{-1}$, respectively. These situations exhibit a wider parameter space with high F_N of reliable set-up, in a way similar to the case of 2000 particles and $\Delta_v = 10 \text{ km s}^{-1}$. This is likely because the smaller number of particles reduce more the effect of the noise for a given Δ_v , and consequently the probability that COSTA finds a spurious structure becomes lower. However, the smaller number of particles also decreases the sampling of the stream and its signal, overall decreasing the signal-to-noise ratio by roughly $\sqrt{N_{\text{part}}}$. This has the consequence that COSTA might not detect the stream with the same efficiency than for higher numbers of particles. Thus, it is essential to test also the detection ability of COSTA as a function of N_{part} , when a stream is present in the detection sample.

3.4.2. Stream detection

We now run COSTA using all set-up configurations with $\text{Re}l \geq 70\%$ over the DS made of the gE0 and dwarf/stream particles, to test the ability of the algorithm to detect cold structures embedded in the hot environment of the central galaxy. We repeat this procedure ten times in order to take into account statistical fluctuations due to a random extraction of the detection sample particles. Furthermore, in order to reproduce a lower limit for the surface brightness of the extracted stream, we impose a minimum number of ten particles to be picked up in an area of about 40 kpc located in the tail of the dwarf. These numbers correspond to a stream with a surface brightness of the order of 28-30 mag arcsec² (see discussion in §4.3)²

² We stress here that this condition has been imposed regardless the N_{part} , which might bias the detection toward intrinsically denser streams for lower N_{part} and, as such, increase the detection power of COSTA for

We note that COSTA does not only detect streams in the proximity of the dwarf, but it also correctly identifies other groups of stream particles, including portions of the stream that are far from the dwarf body. However, these latter detections are fairly occasional because particles that are far from the dwarf have spent more time in the halo of the host galaxies and have started to mix in the phase space of the host halos to be detected as part of a decoupled stream (see discussion in §3.4.4). It is likely that streams detected from COSTA contain, along with the actual dwarf particles, also some contaminants, i.e. particles close to the stream that accidentally also have a similar velocity to that of the particles of the dwarf. This “contamination” is a critical parameter to evaluate because contaminants will alter the inferred stream properties. Since we know, from the simulation, which of the system particles belong to, we will use this information to estimate the contamination fraction (see §3.4.3). Regardless of the mix of the dwarf/stream particles with the background main galaxy particles, we expect that the stream particles closer to the dwarf body are the ones that most keep their kinematics clearly decoupled by the hot background (see also §3.4.4). Among all candidate streams that COSTA recognizes on the DS, we consider as true detections the ones where COSTA correctly identifies at least 4 particles of the stream/dwarf or where at least one third of the total particles (dwarf + contaminants from the main galaxy) are from the stream/dwarf.

The final results of COSTA true positive detections are shown also in Fig. 3. Here we overplot on the density plots, showing the F_N , the combination of parameters where COSTA found the stream (i.e. true positives, red points) and spurious groups (i.e. false positives, cyan points), in the ten repeated DS extractions. In many panels, real (red points) and spurious (cyan) streams cluster in different regions, even though, visually it is not always simple to see this. The most evident case is the $N_{\min} - \sigma_{\text{cut}}$ plot, where red points are slightly shifted towards the right corner, where F_N is higher. More quantitatively, in the $N_{\min} - \sigma_{\text{cut}}$ projection of the case with 2000 particles and $\Delta_v = 40 \text{ km s}^{-1}$, the median F_N for true positive equals 0.88 while that of spurious streams is only 0.73.

Another useful projection which slightly separates real stream from spurious is the $n - N_{\min}$ in the middle of each corner plot. This panel shows the compromise between how strong the sigma clipping can be depending on the minimal number of particles expected in the stream. Indeed a closer inspection of the $n - N_{\min}$ plot reveals that many spurious structures have been detected in the bottom left region, while red points tend to cluster on the upper right. Being more quantitative, the median F_N of red and cyan points in the $n - N_{\min}$ panel are 0.58 and 0.49, respectively.

Thus, in order to minimize the chance of over-collecting spurious streams we adopt a threshold on the F_N in the $n - N_{\min}$ panel. In particular, setting a minimum value of $F_N = 0.5$, we remove about 50% of the spurious structures. We note that, despite the separation is clearer in the $\sigma_{\text{cut}} - N_{\min}$ panel, we prefer to set a threshold in a perpendicular direction of the parameter space, with respect to σ_{cut} in order to reduce the chances to bias the final selection in a projection which is strictly related to stream physical properties. In fact, a further clean involving σ_{cut} might alter the estimated stream kinematics. Since some of the very low F_N regions lie at high σ_{cut} values, removing such regions would rule out all the combination of parameters having

these cases. As we are interested to cover a variety of observational conditions, we keep this condition, however we will take into account the detection efficiency as a function of N_{part} when drawing conclusions.

σ_{cut} close to the actual dwarf velocity dispersion (77 km s^{-1} , see also Table 1).

In the following, we use this threshold as further condition over the detected structures to clean out our list of candidate streams. The effectiveness of this choice will become more clear in §3.4.4.

In Table 2 we report the fractions of set-ups that reveal the stream tail without any false positive, averaged over ten simulations returning at least one detection (i.e. either a true or false positive), with and without applying the threshold of $F_N = 0.5$. We also report the contaminant fraction, which will be defined in §3.4.3.

Generally, the threshold in $n - N_{\min}$ increases the number of set-ups where the stream is recovered. This is particularly evident for the best case with $N_{\text{part}} = 2000$ and $\Delta_v = 10 \text{ km s}^{-1}$ where the fraction of setups returning streams with no spurious is $\sim 67\%$ when applying the threshold of $F_N = 0.5$ in the $n - N_{\min}$ plane and goes down to 0.54 without it. Given the uncertainties, however, this makes very little difference. The same can be said for the impact of changing the number of particles and adopting different velocity uncertainties. Going from 2000 to 1000, keeping Δ_v fix to 40 km s^{-1} F_N goes down from 0.54 to 0.40, but it is always consistent within one- σ errors.

Lower velocity errors tend to shift detected streams towards “more reliable” regions of the parameter space. This is also visible directly from Fig. 3, comparing the top-left and top-right panels and using again the the $n - N_{\min}$ and the $N_{\min} - \sigma_{\text{cut}}$ panels to discriminate between real streams and spurious. Yellow region are more extended in all panels for $\Delta_v = 10 \text{ km s}^{-1}$.

The bottom-left panel of Fig. 3 shows the results of the case 1000-75 giant-dwarf particles and $\Delta_v = 40 \text{ km s}^{-1}$. Here COSTA is still able to detect the stream, even though the ratio of the number of set-ups where the stream has been recovered over the total number of set-ups is the lowest (see column 2 of Table 2), with and without the threshold.

Finally, we consider the case with 500-38 giant-dwarf particles. Here we show the result for $\Delta_v = 20 \text{ km s}^{-1}$ in the bottom-right plot of the same figure. This is, in fact, the precision one can obtain with typical mid resolution spectroscopy. In this case also, COSTA is well able to catch the stream in a quite ample range of configurations in the parameter space ($\sim 50\%$).

In conclusion, for all the different configurations we test, changing the number of particles and the velocity accuracy, COSTA is able to recover the stream in a relatively broad space of parameters (ranging between 40 and 67%). We note that a fifty percent of success is acceptable in blind stream searches, if one wants to find a list of candidates to follow-up, and represents a fair compromise between purity (no false positives) and completeness (i.e. find as many real stream as possible), see also §3.4.3.

3.4.3. Completeness and contamination

We can now better describe and quantify the stream properties as returned by the different set-ups. So far, we have identified the set-up that give the true positives, but every set-up produces different groups of particles, including real stream particles. In particular we can check what is the degree of contamination introduced by the different set-ups with the purpose of finding a method to define the best set-up, e.g. the one optimizing the ratio between number of real particles and contaminators. To do

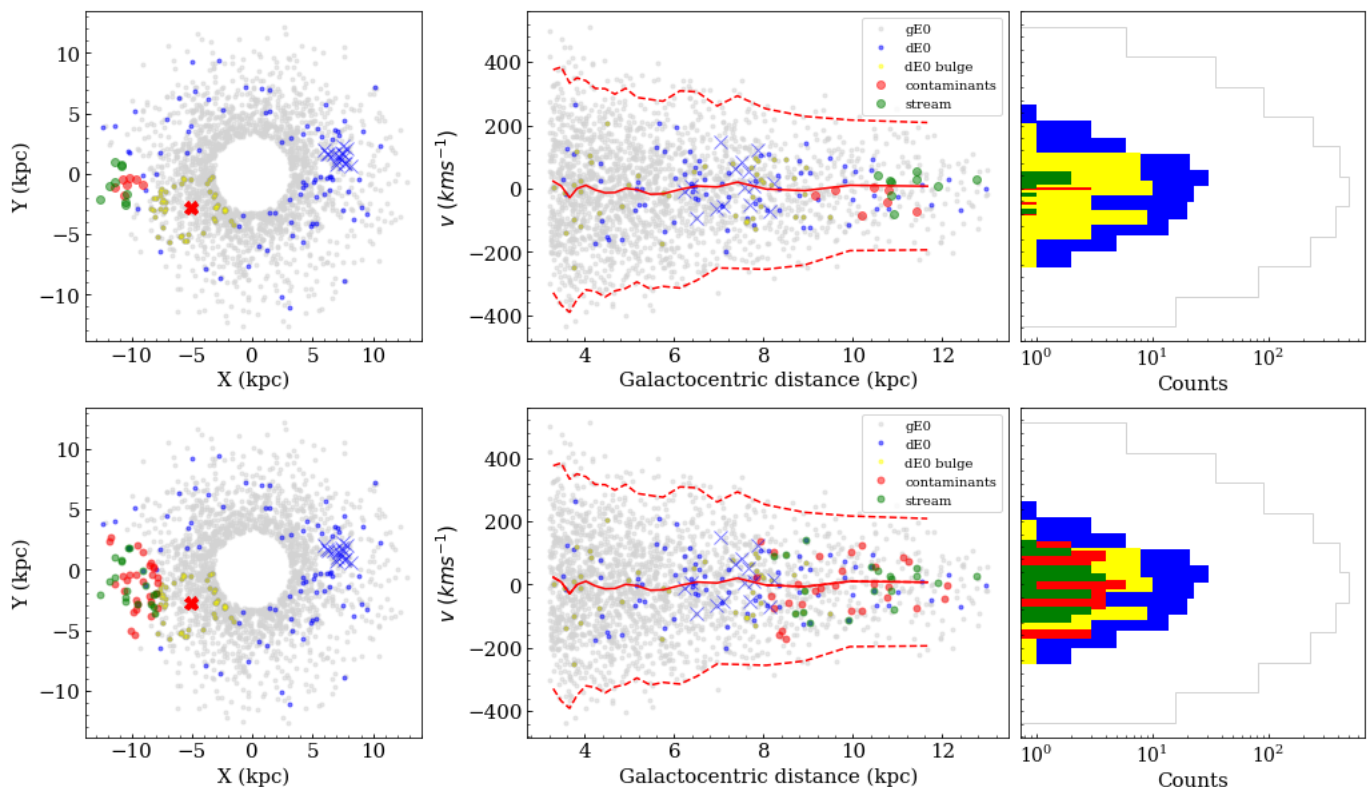


Fig. 4. *Top:* relative positions (left panel) and reduced phase-space (right panel) in the case of the stream recovered with $N_{\min} = 15$. *Bottom:* same as above but with the stream recovered with $N_{\min} = 30$. Light gray points are gE0 particles, while blue ones are those belonging to the dE0. Yellow points represent dwarf particle within 3 effective radii from the dwarf center, while the recovered stream is colored in green (real stream particles) and in red (contaminants).

that, we define the observed completeness (OC), as

$$OC = \frac{\# \text{ recovered stream particles}}{\text{total recovered (stream and non-stream)}}.$$

This parameter is clearly complementary to the contaminant fraction (CF) of the stream (i.e. $CF = 1 - OC$):

$$CF = \frac{\# \text{ recovered non-stream particles}}{\text{total recovered (stream and non-stream)}}.$$

The mean CF derived over the totality of the set-ups producing no false positive (3 column of Table 2) are always $\sim 65-70\%$, almost independently from the sample size and velocity accuracy, which, by definition correspond to $\sim 35-30\%$ of OC. This high fraction of contaminants can significantly affect the conclusion about physical properties of the stream (see e.g. 3.4.4). However, we stress that these quantities are an average over many set-ups and, in principle, one can define the optimal set-up that maximize the OC. We will enter in more details about this optimization in §4.5. We also remark here that the contaminant fraction does not impact the detection of the stream that still remain a good candidate for subsequent follow-ups. These are needed in any cases to obtain the physical properties of the stream (luminosity, colors, surface brightness, kinematics, etc.).

3.4.4. Stream kinematics

Once having demonstrated that COSTA is able to detect a stream, if any, we are interested to extract some physical properties of the recovered stream. In particular, we are interested in deriving some kinematical information of the stream from the

velocities of the tracers collected as part of it. Hence, we want to find some rule of thumb to apply to the many configurations that find the stream, to identify the set-ups which better characterize its kinematical properties (e.g. its velocity dispersion).

Note that a dynamical definition of the stream velocity dispersion is not straightforward, even in simulated samples like Galmer. Technically, the stream is made of all particles left behind by the disrupting dwarf, which have a different degree of mixing, depending on the time they have become unbound. In Fig. 4 we compare the position and velocity distribution of particles belonging to the galaxy background (in grey), the ones belonging to the outskirts of the dwarf galaxy (in yellow, which center is shown as a red cross), and the stream particles (in blue) for one of the runs discussed in §3.4 and two different N_{\min} values ($N_{\min}=15$ top, $N_{\min}=30$ bottom). In the same figure we also plot the true stream particles detected by COSTA in this run (in green), and contaminants that COSTA selected but are instead not part of the true streams (in red). From this figure we can see that the stream particles (blue) overall have a wider distribution with respect to both the dwarf body particles (yellow) and the ones that COSTA detects in the proximity of the dwarf (red and green), while they are not as dispersed as the gray particles of the central galaxy halo. As such, they are both unbound to the parent dwarf and unmixed to the host halo, hence their velocity dispersion does not have a dynamical meaning because hydrostatic equilibrium does not hold. On the other hand, the “youngest” regions of the stream (green particles) show a distribution which is similar to the ones of the dwarf particles (yellow) that are at the equilibrium. Thus, the particles recently lost in the tail (and more likely detected from COSTA) keep the record of the kinematics

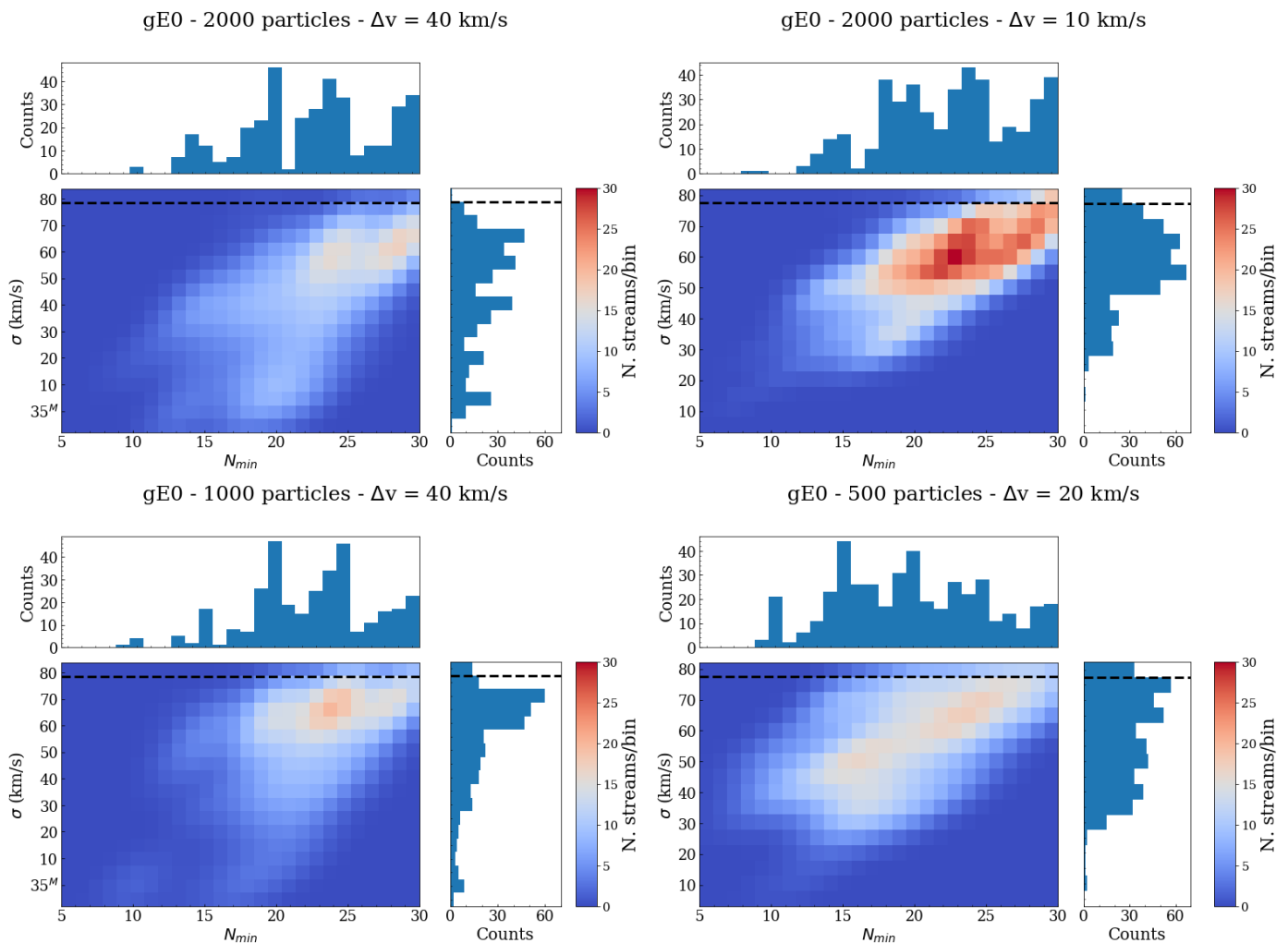


Fig. 5. Density plot of the number of set-ups with a reliability above the selected threshold and with $F_N (\geq 0.5)$ in the $n - N_{\min}$ space. Data have been smoothed with a Gaussian kernel having a bandwidth equal to 3 bins.

of the parent galaxy³. This means that these latter particles have not yet fully dynamically decoupled from their progenitor and we are dynamically motivated to compare their velocity dispersion with the dwarf velocity dispersion (i.e. 77 km s^{-1} , see table 1). This is useful for two main reasons: 1) algorithm-wise this is the best way to identify set-ups that better describe some (dynamical motivated) kinematical properties of a detected stream; 2) dynamically-wise we postulate that the stream velocity dispersion should follow the Faber-Jackson (Faber & Jackson 1976) of the parent dwarfs, i.e. the velocity dispersion should correlate with the luminosity of the progenitor, if any.

To illustrate how this works on data, looking at Fig. 4 again we clearly see a typical situation of a stream detection where stream particles (including some contaminants) are close to the bulk of the parent galaxy.

For both the case with $N_{\min}=15$ and that with $N_{\min}=30$, COSTA selects only a limited fraction of particles and very close to the dwarf (tail). The ratio of the red particles over all red+green gives the OC, which decreases towards higher N_{\min}

³ Dynamically speaking this means that both the energy transfer from orbital momentum to the dwarf GCs (e.g. via tidal approximation, see Napolitano et al. 2002) and the dynamical friction ($\propto \rho/\sigma_{\text{env}}^2$, where the density, ρ and the inverse of the velocity dispersion $1/\sigma_{\text{env}}^2$ of the environment are small), have a minor impact on the stripped particles.

(e.g. 0.56 vs 0.40). On the contrary, the overall velocity dispersion increases from the $N_{\min} = 15$ to 30 (as seen in both the phase-space diagram – the velocity-radius plot in the middle panels – and the velocity histogram in the right panels) and, in the latter case, it becomes closer to the one of the dwarf (i.e. 77 km s^{-1}). Green and red particles have rather similar velocity dispersion values, i.e. (40 and 74 km s^{-1} - green, 35 and 83 km s^{-1} - red for the recovered stream respectively with $N_{\min} = 15$, top row, and with $N_{\min} = 30$, bottom row). This suggests that the contaminants only slightly alter the true velocity dispersion of the stream.

Only in a very few runs, COSTA also detects groups of particles in the tail of the stream that are further away from the dwarf main body, on the opposite side of the central galaxy (see e.g., blue crosses in Figure 4). This shows that COSTA can, in principle, identify also portions of the debris of a stream in absence of a close dwarf (e.g. at the pericenter/apocenter of stream orbits where lost particles tend to accumulate around zero systemic velocity in the reference frame of the central galaxy). This is due to the fact that, being stream (blue) particles still unmixed to the halo, they are also recognized as cold substructures.

The fact that the majority of the detections occur in the regions close to the galaxy depends strongly on the fact that these particles are fully unmixed. For a detection at larger distances to occur, one needs an *ad-hoc* combination of poor mixing and

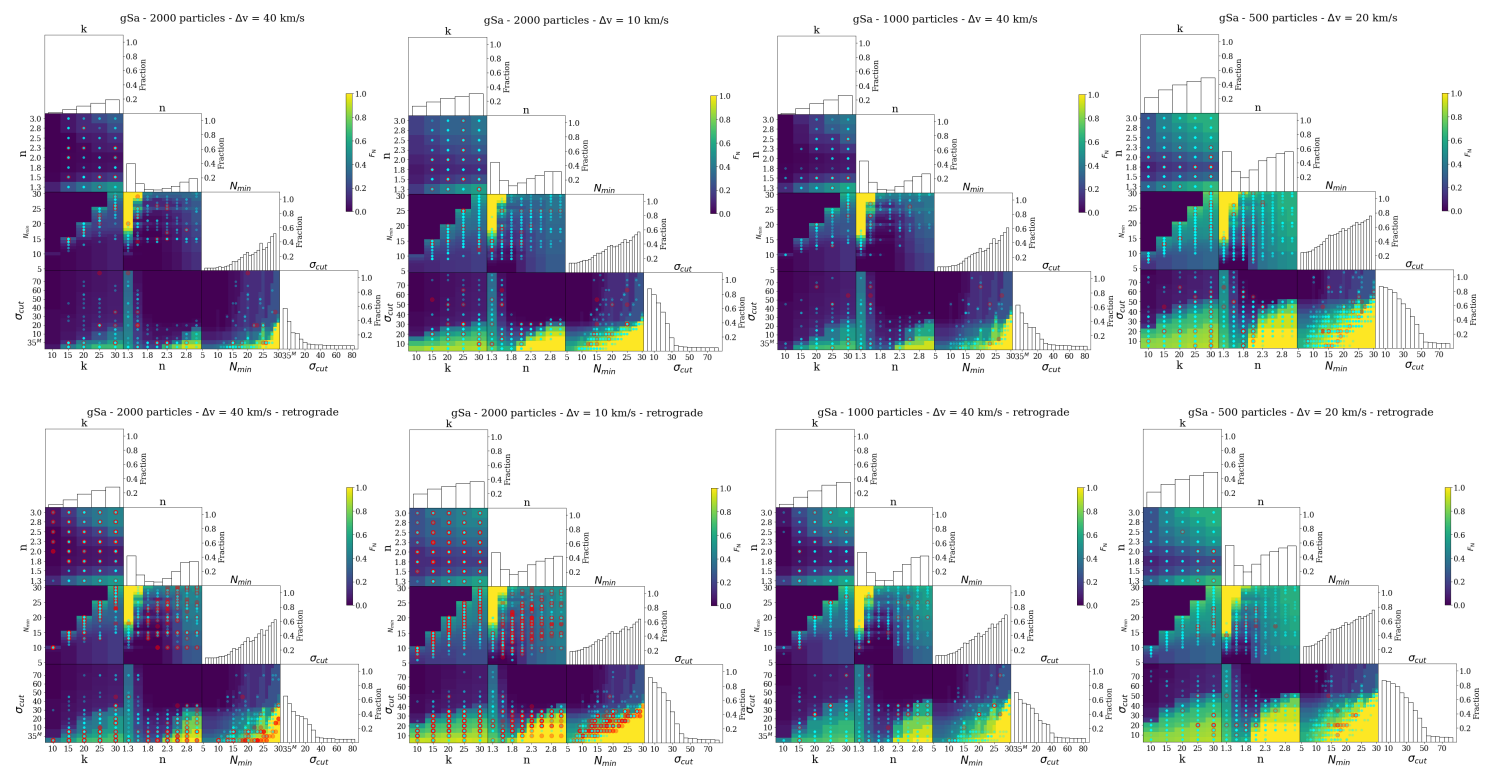


Fig. 6. Same of Fig.3 but for the gSa in the prograde and retrograde encounter.

occasional overdensity, which is more difficult to happen. It remains that the velocity dispersion of these latter detections cannot be dynamically connected to the parent dwarf (e.g. via Faber-Jackson relation). The only case one is motivated to dynamically interpret the velocity dispersion of an isolated group of particles that has no clear dwarf association is in the case there are evidence that the parent dwarf has been recently disrupted and the remaining particles are the latest lost.

Finally, since we have postulated a connection between the kinematics of the stream and the one of the parent dwarf (e.g. a sort of stream Faber-Jackson), and given that COSTA can detect the same stream with different configurations, we are interested to check whether we can identify configurations that reproduces as close as possible the real internal dispersion of the dwarf. In Fig. 5 we show the density plot of the velocity dispersion estimates of the selected stream particles as a function of the most sensitive parameter discussed in this paragraph, N_{\min} . In particular, we show the values obtained using a threshold on $F_N = 0.5$ in the $n - N_{\min}$ space as described in the §3.4.2.

The four plots correspond to the measured velocity dispersion, σ_{mea} , from the streams selected according to the four different cases as in Fig. 3. Overall, we notice that the velocity dispersion estimates tend to cluster around the true value of the dwarf (77 km s^{-1}), with tails towards lower values. This happens regardless of the sample size and velocity errors, although the higher velocity accuracy (e.g. $\Delta v \leq 10 \text{ km s}^{-1}$, top right panel, and $\Delta v \leq 20 \text{ km s}^{-1}$, bottom left panel) give less pronounced tails toward low σ_{mea} in the velocity distribution. This is particularly evident when comparing the 2000-particles cases (top row of Fig. 5).

Being more quantitative, using the median of the distribution as probe of the peak, we obtain the following stream velocity dispersions: $43 \pm 23 \text{ km s}^{-1}$, $57 \pm 12 \text{ km s}^{-1}$, $57 \pm 15 \text{ km s}^{-1}$,

$57 \pm 18 \text{ km s}^{-1}$, for the 2000 (40), 2000 (10), 1000 (40) and 500 (20) cases respectively.

Of course, the final dispersion of the stream in all cases is affected by the contaminants from the main galaxy, but overall the median values are always consistent within $1-\sigma$ uncertainties and all close, although slightly lower, to the true velocity dispersion of the dwarf. This implies that the contaminant selected by COSTA as part of the stream are almost statistically indistinguishable from the stream particles as they hold a similar overall kinematics (see Fig. 4).

3.5. The case of gSa-dS0 encounter: testing COSTA on a cold system

Having demonstrated that COSTA is able to find cold streams embedded in the halo of hot early-type systems, we now need to test the case of late-type galaxies. We select a gSa-dS0 encounter, and test both a prograde and a retrograde motion for the dwarf, because the stronger rotation of the galaxy disc might have a different impact in the two cases. We follow the same steps as in the gE0-dE0 case, and we highlight the results in the following sections.

3.5.1. Reliability

First we run COSTA over the WNS using all parameter combinations to determine the reliability distribution in the parameter space. In Fig. 6 we show the reliability maps for the prograde and retrograde cases, on two separate rows. Also in this case, we show the density plot obtained with different number of particles for the giant and the dwarf and different values of Δv .

Since the gSa is colder than the gE0, it is much easier for COSTA to find combinations of galaxy particles with a local ve-

Table 3. Same of Tab. 2 but in the case of the spirals.

gSa-dS0 Prograde	F_N	CF
2000 part - 40 km s ⁻¹	0.10 ± 0.13	0.61 ± 0.14
^a 2000 part - 40 km s ⁻¹	0.14 ± 0.20	0.74 ± 0.15
2000 part - 10 km s ⁻¹	0.08 ± 0.15	0.57 ± 0.15
^a 2000 part - 10 km s ⁻¹	0.11 ± 0.19	0.67 ± 0.19
1000 part - 40 km s ⁻¹	0.04 ± 0.06	0.73 ± 0.13
^a 1000 part - 40 km s ⁻¹	0.04 ± 0.12	0.89 ± 0.11
500 part - 20 km s ⁻¹	0.03 ± 0.04	0.71 ± 0.12
^a 500 part - 20 km s ⁻¹	0.04 ± 0.05	0.73 ± 0.16
gSa-dS0 Retrograde	F_N	CF
2000 part - 40 km s ⁻¹	0.14 ± 0.22	0.13 ± 0.14
^a 2000 part - 40 km s ⁻¹	0.11 ± 0.19	0.26 ± 0.17
2000 part - 10 km s ⁻¹	0.29 ± 0.34	0.16 ± 0.15
^a 2000 part - 10 km s ⁻¹	0.14 ± 0.21	0.26 ± 0.12
1000 part - 40 km s ⁻¹	0.04 ± 0.12	0.36 ± 0.14
^a 1000 part - 40 km s ⁻¹	0.03 ± 0.09	0.44 ± 0.19
500 part - 20 km s ⁻¹	0.04 ± 0.05	0.57 ± 0.10
^a 500 part - 20 km s ⁻¹	0.03 ± 0.04	0.50 ± 0.13

a: in these configurations we ruled out set-ups with $F_N < 50\%$ in the $n - N_{\min}$ space as described in the text.

locity dispersion close to that of the σ_{cut} (i.e. there is a smaller contrast). It is much easier that COSTA find spurious substructures and consequently harder to find set-ups with high reliability (i.e. with more than 70% of no-spurious detections). As a result, the regions of the parameter space with high F_N (yellow) are considerably reduced with respect to the gE0 case, and there is generally a higher chance to find some false positive.

As for gE0, the adoption of smaller velocity errors produces a slightly wider number of good set-ups, especially in the retrograde case, and the F_N increases over a relatively wider area, also for the smallest number of tracers tested in our simulations (4-th panel).

The results for the prograde (top) and retrograde (bottom) cases are very similar, substantially because in the two cases the WNS does not change dynamically in a significant way, despite the different interaction with the intruder might have introduced different perturbations.

3.5.2. Stream detection

The second step is to run COSTA on the DS, made by the main galaxy and dwarf particles, to recover the stream particles. As done for the gE0+dE0 encounter, we perform ten random extractions of the giant+dwarf system, imposing a limit on the lower surface brightness of the stream. The results of this test are listed in Tab. 3, both for the prograde and the retrograde encounters. In general, COSTA detects the stream only in few set-ups with reliability $\text{Rel} \geq 70\% \geq 70\%$ both for the prograde and retrograde motions. Furthermore, in the gSa-dS0 case, most of the set-ups which correctly found the stream particles, also detect spurious substructures (see bottom left panel of Figure 6 or Table 3).

Overall, for the retrograde encounter COSTA performs better, with a much lower CF (e.g., ~ 15% versus ~ 60% for the 2000 particles case with $\Delta_v = 40 \text{ km s}^{-1}$). The number of set-ups in which COSTA detects a stream is also higher in the retrograde case, at least for the best possible configuration, i.e. 2000 part - 10 km s⁻¹ (11% for the prograde and 29% for the retrograde, assuming a threshold of 50% in the $n - N_{\min}$ panel, although with a large uncertainty). In this configuration, and partially also in that

with 2000 particles and larger velocity error, the stream has been detected in regions that tend to accumulate toward the high F_N (yellow areas) of high-reliability in the parameter space. This is especially visible in the $N_{\min} - \sigma_{\text{cut}}$ plot, as we have seen for the gE0 system. In particular, high-reliability configurations favor smaller $\sigma_{\text{cut}} (\leq 40 \text{ km s}^{-1})$. However, this is not always true for the prograde cases and the retrograde cases with a smaller number of particles, at least not for all the projections. In these cases, the stream has been detected only few times and they are very sparse in the region of the single plots of the parameter pairs.

Finally, as seen in Fig. 6, at least for the retrograde case, COSTA performs generally better when the velocity errors are smaller. Here, the algorithm reveals the stream in more set-ups.

An interesting difference between the gE0-dE0 case and the gSa-dS0 is that, for the latter, the number of particles makes a much larger difference in terms of number of set-ups with high reliability. And this valid both for the prograde and for the retrograde case. Going from 2000 particles to 500, the F_N is between 3 and 5 times smaller while the CF increases.

We also note that, for the gSa-dS0 cases, and in particular for the prograde encounters, the configurations for which we correctly detect the streams are often embedded in low- F_N areas. This is different from what happens in the gE0-dE0 interaction and it is because, since COSTA finds more spurious, the configurations that allow to find the stream also find some spurious, at least with the change of other parameters. This means that, even if the stream is found, this has a general lower reliability in cold systems. We need to stress here that this conclusion is not general, as this applies to the case of a mass ratio 10:1, i.e. with a small contrast between the dispersion of the stream and the dispersion of the background velocity field (see below).

3.5.3. Stream kinematics

The $\sigma_{\text{cut}} (\leq 40 \text{ km s}^{-1})$ is an upper limit beyond which COSTA does not detect the stream anymore. The median of the velocity dispersion, using only set-ups with $F_N > 0.5$ in the $n - N_{\min}$ plot in the retrograde encounter, gives a velocity dispersion that is lower than the one of the parent dwarf galaxy ($\sigma_{\text{dwarf}} = 74 \text{ km s}^{-1}$). In fact, we obtain as median of the velocity dispersion distributions: $24 \pm 13 \text{ km s}^{-1}$, $31 \pm 7 \text{ km s}^{-1}$, $33 \pm 2 \text{ km s}^{-1}$, $37 \pm 6 \text{ km s}^{-1}$ for the 2000(40), 2000(10), 1000(40), 500(20) cases.

Here the worse performance of COSTA with respect to the gE0-dE0 is due to the little contrast of the dwarf velocity field (which is rather hot in the specific Galmer simulation, i.e. $\sigma_{\text{dwarf}} \sim 74 \text{ km s}^{-1}$), with respect to the gSa ($\sigma_{\text{giant}} \sim 81 \text{ km s}^{-1}$).

Thus, the exercise we carried on here has therefore to be interpreted as an “extreme case” to set a guideline for the methodology to follow in “real” cases, where the difference between the velocity dispersion of the dwarf and that of the giant is larger.

3.6. The dependence of the performance of COSTA on the reliability threshold

In this section we explore how a different reliability threshold can affect the completeness and purity of COSTA. Overall, logically, a lower threshold allows us to rise the probability to find a stream, at the expense of a greater contamination, while an higher limit has the opposite effect.

In the case of the gE0-dE0 interaction, we increase the lower limit of the reliability and we use only combinations of free parameters above 90%. We run COSTA only on the $N_{\text{giant}} = 2000$, $N_{\text{dwarf}} = 150$ and $\Delta v = 40 \text{ km s}^{-1}$ configuration. Of course, the

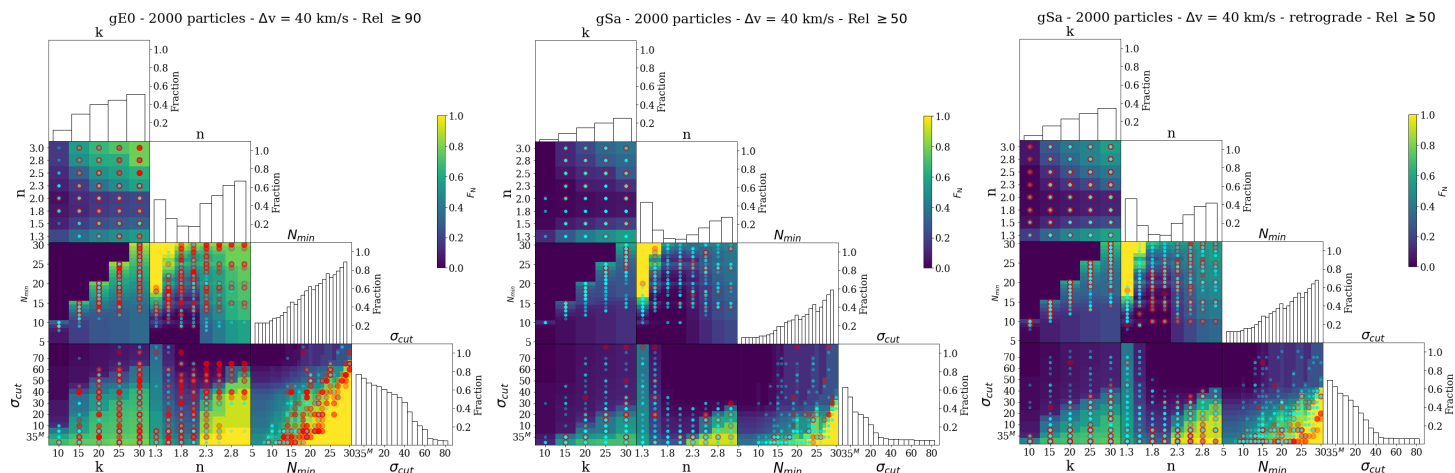


Fig. 7. Parameter space overlapped with stream and spurious detected by COSTA for both early and late type galaxies, in the standard configurations (2000 particles and $\Delta v = 40 \text{ km s}^{-1}$) for the three cases (gE0, gSa prograde and gSa retrograde), but using different reliability thresholds.

number of parameter combinations which overcome the threshold are reduced with respect to the previously used threshold of 90%. This can be seen in left panel of Fig. 7 (left panel). However, the stream is still detected in many set-ups, and they show almost the same distribution in the parameter space as for the lower threshold.

For the gSa-dSa interaction the situation is reversed, as we lower the acceptable value of reliability to 50%. Indeed, in both the prograde and retrograde encounters, COSTA could not find streams using a higher threshold, so we check a lower one. We use, in both encounters $N_{\text{giant}} = 2000$ and $N_{\text{dwarf}} = 150$ and $\Delta v = 40 \text{ km s}^{-1}$. In the prograde case (central panel of Fig. 7), COSTA finds the stream in a slightly larger number of set-ups, with respect to the very few ones with a reliability cut-off of 70%. In the retrograde case (right panel of the same figure) the improvement is even higher as the number of set-ups where COSTA detects the stream increases by 50% with respect to the previous case. Thus, we conclude that for the late-type case, the 70% reliability threshold is too conservative and a lower reliability threshold would give more chances to identify streams.

4. The case of the Fornax cluster core

We test now COSTA on a cluster environment, where streams are produced in a more complex situation with many large coexisting galaxies. In such environment, multiple low surface brightness streams from a larger population of dwarf galaxies, with a given luminosity function and different kinematics properties, can be produced.

In particular, we present here the case of the Fornax cluster, for which there are GCs (from P+18) and PNe (from S+18) available for stream search, that we will present in forthcoming analyses.

The aim of this section is to show that also for a more complex case, as the Fornax cluster core, COSTA can be set to detect cold streams of small number of particles, as done for the Galmer simulations.

For the Fornax cluster, unfortunately, we do not possess a simulation realistic enough to produce the same large structure distribution of particles as reported in GCs and PNe studies. We thus decide to build up Montecarlo realizations of the kinematical tracer distribution in the 3D phase space (i.e. 2D positions and radial velocity) over which we can obtain a reliability map for COSTA and test its stream detection performances.

Indeed, following the approach adopted for the Galmer simulations, the Montecarlo realizations of the Fornax core are needed, first, to have a smooth cluster background with no streams (i.e. the WNS). This allows us to explore the parameter space and assess the reliability function of COSTA as a function of the different parameters. Second, we add a number of artificial streams (hence generating different DSs) and run COSTA to recover them and to calculate the OC and CF.

4.1. Montecarlo simulations of the Fornax cluster core

To produce COSTA reliability maps, we perform a suite of Montecarlo simulations, which reassemble the Fornax core as close as possible, in terms of spatial distribution, local density and radial velocity distribution of the kinematical tracers (WNS).

We simulate only the region covered by the current discrete tracer surveys (FVSS, P+18 and S+18), covering about 1.8 deg^2 around the cD, NGC 1399. In this area, there are two other bright early-type galaxies: NGC 1404, located just below the cD, in the S-E direction at about 9 arcmin; and NGC 1387, at a distance of ~ 19 arcmin in the West direction from NGC 1399. A third relatively massive galaxy, NGC 1379, located at $\sim 60'$ toward W, has been observed with one FORS2 pointing in S+18. However, this system is excluded by this analysis because we do not have continuity with the rest of the Fornax core area, hence it is useless for stream finding.

We generate simulated GCs and PNe in a number that is as close as possible to what has been observed in S18 and P18. In the following, we assume that both GCs and PNs trace the same underlying population of old stars⁴, at the equilibrium in the gravitational potential of these three galaxies, assumed to be the superposition of the individual galaxy potentials with spherical symmetry. Following Napolitano et al. (2001), we produce the 3D position starting from a 3D spherical density profile and projected them on the 2D sky plane (X-Y in our case). For each particle, we determine the 3D velocity vector, according to the hydrostatic equilibrium equations (see below), which we project along the line of sight to derive the intrinsic radial velocity. We finally simulate a radial velocity measurement by randomly extracting the measured velocity from a Gaussian having the truth

⁴ For a discussion about the statistical similarity between the two tracers, see Napolitano et al. in preparation.

radial velocity as mean and standard deviation equal to the measurement errors.

In order to produce these Montecarlo realizations of particles sampling the total potential in the Fornax core, we assume for the cluster a total mass of about $10^{14} M_{\odot}$ and a Hernquist (Hernquist 1990) density distribution of the stellar-like tracers. This is a good approximation for elliptical galaxies following a de Vaucouleurs law (1948). Indeed, for NGC 1399, which gathers most of the light in the cluster core, Iodice et al. (2016) found a Sersic index $n = 4.5$, i.e. very close to $n = 4$, describing the de Vaucouleurs law.

The luminous mass density is expressed by the formula

$$\rho(r) = C \frac{M_1 a}{2\pi} \frac{1}{r(r+a)^3} \quad (3)$$

where M_1 is the total luminous mass, a is a distance scale ($R_e = 1.81534 a$) and C is a normalization constant. We make the same assumption for all other galaxies in the area, with the adopted parameters as in Table 4.

In addition to the stellar mass density, we also consider a dark halo following a Navarro-Frenk-White profile (NFW) (Navarro et al. 1997), to define a realistic internal kinematics for the simulated particles. Hence, the potential of the system at equilibrium is provided by the total mass:

$$M_{\text{tot}} = M_1 + M_{\text{dm}} \quad (4)$$

We assume no-rotation⁵, and an isotropic velocity dispersion tensor, and solve the radial Jeans equation

$$\frac{d(\rho\sigma^2)}{dr} = -G \frac{M_{\text{tot}}(r)\rho(r)}{r^2} \quad (5)$$

to derive the 3D velocity dispersion σ^2 along the three directions in the velocity space, and generate a full 3D phase space.

As briefly anticipated above, we simulate an observed phase-space by projecting the tracer distribution on the sky plane and derive the line-of-sight (LOS) velocity of the individual particles. In particular, we use the X-Y plane as sky plane and Z-axis as the LOS. However, due to the full spherical symmetry of the model, the particular projection is irrelevant.

Finally, in order to simulate a velocity measurement, we use the same approach as for the Galmer simulations: we adopt a Gaussian error distribution and re-sample the radial velocities produced by the Montecarlo simulations with a $\Delta_v = 37 \text{ km s}^{-1}$, consistent with typical measurement errors from P+18 and S+18. In this case we do not vary the errors, as this test is meant to demonstrate that COSTA can be applied on a real dataset and provide a series of reliable set-up to find stream candidates from real datasets in hands, as we will do in the second paper of this serie.

We include in the simulation 1985 particles, to reproduce as much as possible the number of observed PNe and GCs selected in the area.

The number of points for each satellite galaxy is then obtained with a cross-match with the real data, counting the number of plausible PNe and GCs bound to the galaxies, while both effective radii and velocity dispersion are taken from literature (see Table 4).

⁵ Although some rotation of blue GCs in the radial range between 4 and 8 arcminutes was measured, the kinematics of the outskirts of NGC 1399 is dominated by the random motion (Schuberth et al. 2010; Coccato et al. 2013)

Table 4. Parameters of the simulated galaxies. The effective radii are taken from the literature, unless differently specified. The velocity and velocity dispersion values are retrieved from the Nasa Extragalactic Database (NED), unless differently specified.

Galaxy	Number of Points	R_e (arcsec)	Vel. (kms^{-1})	σ_p (kms^{-1})
NGC 1399	1855	138	1425	320
NGC 1387	90	42	1302 ^a	160
NGC 1404	40	100 ^a	1947	247

a: Values adopted to obtain a more realistic reproduction (see text).

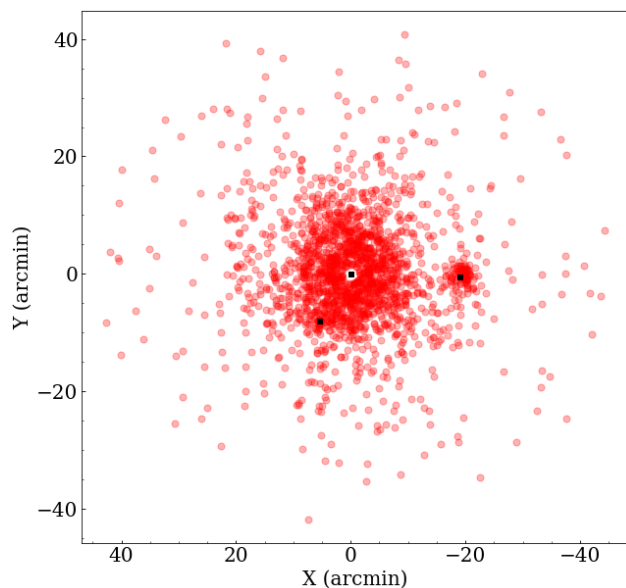


Fig. 8. Simulated datapoints for one of the Montecarlo realizations, with NGC 1399 at the origin of coordinates. NGC 1404 is just below the cD ($X \sim -5$, $Y \sim -5$) and NGC 1387 is at $X \sim -20$ arcmin. The positions of the three galaxies are indicated by black squares.

To obtain a realistic reproduction of the PN and GC systems around NGC 1404 (in terms of number and radial abundance), we need to adopt an effective radius (i.e. the radius enclosing half of the total light of the galaxy), $R_e \sim 100''$, slightly larger than the one estimated by Corwin et al. (1985) ($R_e \sim 80''$).

For NGC 1387, we take into account the velocity offset of PNe reported by S+18 (i.e. a mean velocity higher by $\sim 100 \text{ km s}^{-1}$ than the systemic velocity of the galaxy reported in literature). Indeed in this area, we have a larger number of PNe than GCs, respectively 117 (88%) and 16 (12%) within three effective radii from NGC 1387; thus the offset of the PN velocities might generate an overall velocity excess of 100 km s^{-1} , that we thus artificially add to all simulated points around NGC 1387 in order to match the real objects, see also Table 4.

The final result of all these fine-tuning calibrations for the simulated sample gives the distribution of the simulated particle as shown in Fig. 8. Here, we plot the simulated points for one of the mock realizations with positions computed with respect to the simulated cluster center. We observe a fair spatial correspondence between the main galaxies in the field of view (whose positions are highlighted as black squares) and the simulated particles (red points).

In Fig. 9, we show the phase-space distribution of the same simulated particles together with the $\pm 3\sigma_p$ profiles (where σ_p is

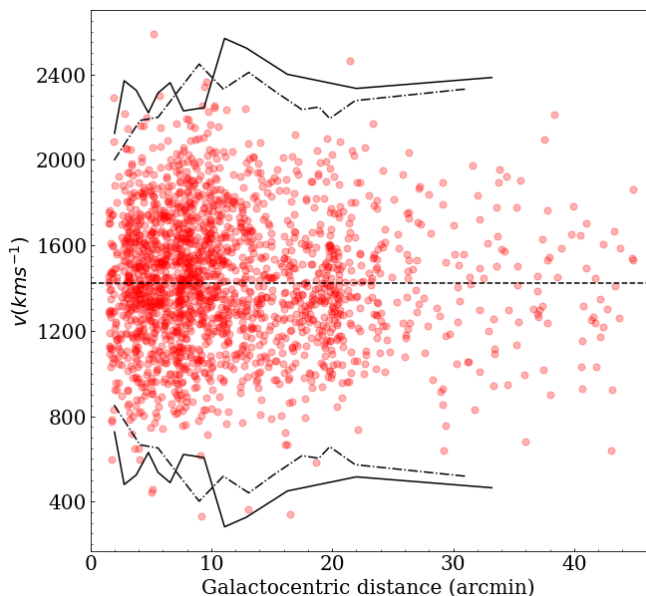


Fig. 9. Phase-space of one of the Monte Carlo simulations. We plot on the x-axis the distance from NGC 1399 in arcminutes and on the y-axis the velocities of the points in km s^{-1} . The continuous solid and dashed-dotted lines represent the $\pm 3\sigma_p$ profiles of the GCs and PNe, respectively, extracted from P+18 (their Fig. 9). The dashed black horizontal line represents the systemic velocity of NGC1399 (1425 km s^{-1})

obtained as in Eq. 1) of the GCs from P+18 and the PNe from S+18 (curves are extracted from Fig. 9 in P+18). Once again the similarities are quite evident between the overall kinematics of the simulated particles and of the observed ones.

Once optimized the Monte Carlo simulation set-ups to best reproduce the observed GC+PN dataset, we finally produce 100 realizations of the system, that represent the WNS from which we obtain the reliability maps for COSTA.

Differently from the Galmer simulations, where the statistical variation of the parameters have been obtained only perturbing the velocities of the particles, for the Fornax-like case we re-sample the full parameter space. Hence we add more statistical noise to the simulated sample, coming from different spatial configurations of the same physical streams.

4.2. COSTA set-up and reliability map

To obtain the reliability map, we follow the same steps as in the Galmer simulations (§3.4 and 3.5). To begin, we run COSTA for each parameter combination over the 100 Monte Carlo realizations of the WNS and count the number of configurations for which COSTA finds no spurious streams.

In this case we uniformly sample the k , n , N_{\min} parameters space, for different σ_{cut} and run COSTA with all the possible combinations of the free parameters selected in the following ranges:

- k : from 10 to 50 with steps of 5
- n : from 1.3 to 3 with steps of 0.2-0.3
- N_{\min} : all values from 5 up to k
- σ_{cut} : from 10 to 120 km s^{-1} with steps of 5 km s^{-1} .

The difference with respect to the gE0-dE0 case (i.e. the case of another hot systems), is the adoption of larger σ_{cut} , k , and a larger N_{\min} range. This is motivated by the fact that, being

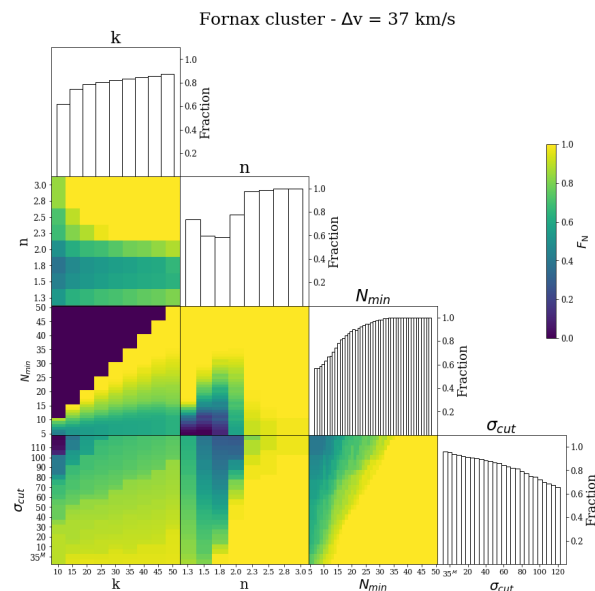


Fig. 10. Reliability map for the Fornax cluster obtained with a reliability threshold of 70%.

the Fornax environment hotter than the Galmer gE0, we can detect higher velocity substructure (if any). Similarly to the Galmer simulations, we use also σ_{cut} values below the instrumental errors, considering in these cases $\sigma_{\text{mea}} \sim \sigma_{\text{obs}}$ (see discussion in §3.4).

Fig. 10 shows the reliability map, color coded by the fraction of the number of set-ups with a reliability $\geq 70\%$. The case of the Fornax-like system is fairly different with respect to the configurations tested with the Galmer simulation. Indeed, the intrinsically higher velocity dispersion provides a much smaller chance to have a correlated group of particles characterized by a small dispersion, due to statistical fluctuation in the parameter space. For this reason, COSTA has a quite large range of parameters that find a spurious stream in less than 30% of the extractions. One would argue that maybe for this case 70% is a too loose threshold and higher values might be used too. However the Monte Carlo simulations are only partially catching the full statistical fluctuations, and they might be too smooth with respect to the real data. In conclusion, also taking into account that the higher is the threshold the lower is the chance to find a stream, we keep 70% as reliability threshold, in line with the previous tests.

As a second step, we run COSTA on the DS where the artificial streams have been added, to assess the effectiveness of COSTA detection.

4.3. Recovering simulated substructures

When applying COSTA to real cases, detection is the minimal goal we want to achieve (completeness), while we can compromise with the full recovery of stream particles vs. contaminants (purity), as we reasonably expect that we lose some particles and also get some contaminant (non-stream particle) as part of a correctly detected stream (see also the discussion in §3.4 and §3.5).

To check the ability of COSTA in recovering known streams in the Fornax-like environment, and assess completeness and purity, we add three artificial streams to our Monte Carlo simulations. Since we cannot reproduce the full dynamics of a stream

Table 5. Properties of the simulated streams

	N	Size (arcmin)	σ_I (kms ⁻¹)	σ_M (kms ⁻¹)
<i>stream 1</i>	20	2 X 1	35	42
<i>galmer 1</i>	30	3 X 1.5	45	58
<i>galmer 2</i>	30	6 X 3	62	69

in our Montecarlo simulations, and we want to test COSTA into more observational situations, we choose typical stream sizes and kinematics that can be realistically found in real data. As shown in the case of Galmer simulations (see e.g. Fig. 4), despite a dwarf galaxy spreads a large number of particles along its encounter orbit, COSTA can identify only the closer ones, that were the last to be stripped (of the order of a few tens, depending on the surface brightness of a stream), spread over ~ 5 – 15 kpc, i.e. $1'$ – $3'$ at the distance of Fornax.

A first stream (*stream 1*, hereafter), is made of 20 particles, has the size of $1' \times 2'$ and an intrinsic velocity dispersion of $\sigma = 35$ kms⁻¹. Other two streams are extracted by randomly sampling particles from the tail of the Galmer gE0-dE0 case discussed in §3.4. We isolate a group of 30 particles, distributed over an area of about $3' \times 1.5'$ in one case (*galmer 1*, hereafter) and $6' \times 3'$ in a second case (*galmer 2*), with an intrinsic velocity dispersion of $\sigma = 45$ kms⁻¹ and $\sigma = 62$ kms⁻¹, respectively. These two streams have the advantage of being more realistic (in shape and density) as based on a simulated encounter, although the dynamics of the Galmer simulation adopted is not really close to the one of the Fornax core, in particular because of the smaller mass of the main galaxy as compared to NGC 1399. Also, we take larger sized streams ($3'$ roughly correspond to 30 kpc), in order to explore the ability of COSTA to find larger and more diffuse streams.

The final properties of the artificial streams are summarized in Table 5.

In order to simulate a real measurement of the particle redshift, we randomly re-extract their “measured” velocities from a Gaussian having the central velocity equal to the intrinsic radial velocity, and standard deviation of 37 kms⁻¹. We stress here that the three streams have a velocity dispersion within the range expected for dwarf galaxies (Kourkchi et al. 2012).

Also, the number of particles is not arbitrary: indeed, assuming that we split the particles in the same number of PNe and GCs, and assuming a typical (bolometric) PN specific number density of 50×10^{-9} PN/ L_{\odot} (see e.g. Feldmeier et al. 2004), the luminosity in *g*-band corresponding to 10-15 PN-like particles is of the order of $10^8 L_{\odot}$. The corresponding surface brightness of streams, with sizes as in Table 5, is of the order of 28-29 mag/arcsec², which is close to the typical low surface brightness levels expected for these substructures (see e.g. Cooper et al. 2010).

At this point, we build a set of Montecarlo simulations to which we add the particles of the three simulated streams each time varying their mean velocity in a random way, using a Gaussian with a 0 kms⁻¹ mean, assuming the cD at rest in the cluster center, and with a standard deviation of 300 kms⁻¹, similar to the velocity dispersion of the Fornax cluster (see P+18 and S+18 for a discussion). We also randomize every time their positions to recover them in three different ranges of cluster-centric radii, in order to verify a dependence of the recovery rate with the distance (and hence the local particle density). We choose three shells: $R = 5' - 7'$, $R = 7' - 12'$, $R = 12' - 18'$, while we exclude the region within $5'$, where the light is too dominated by the cD and it would be very hard to detect low surface brightness structures.

Table 6. Same of Tab. 2 but in the case of artificial streams in a Fornax-like cluster.

Stream	F_N	CF
$R = 5' - 7'$		
<i>stream 1</i>	0.69 ± 0.07	0.26 ± 0.18
<i>galmer 1</i>	0.66 ± 0.22	0.24 ± 0.12
$R = 7' - 12'$		
<i>stream 1</i>	0.69 ± 0.06	0.18 ± 0.15
<i>galmer 1</i>	0.78 ± 0.09	0.22 ± 0.18
<i>galmer 2</i>	0.68 ± 0.15	0.20 ± 0.15
$R = 12' - 18'$		
<i>stream 1</i>	0.60 ± 0.19	0.17 ± 0.15
<i>galmer 1</i>	0.77 ± 0.08	0.18 ± 0.18
<i>galmer 2</i>	0.74 ± 0.10	0.15 ± 0.14

We do not put the streams at distances larger than $18'$ in order to be conservative, as in less dense regions the frequency with which the stream is recovered could be overestimated because of a lower background. Furthermore, the stream *galmer 2* has been inserted only in the two external shell because this diffuse stream is typical of longer lived passages happening far from the cluster center (see e.g. the tail of the encounter in Fig. 1).

As for the Galmer systems, we run COSTA on 10 over 100 of the Montecarlo simulations from the reliability run, to evaluate the stream detection performances. The results for the three streams at different radii and their reliability maps are displayed in Fig. 11 and listed in Tab. 6.

The general result is that COSTA is able to recover all streams with a broad number of set-up parameters. On average, for the *galmer* streams, the recovery slightly increases at larger distances mainly because the signal from the particles belonging to the stream is higher with respect to the noise of the hot environment (with lower local density). This does not happen for the *stream 1*, which is smaller and more compact. Specularly, the contaminant fraction decreases with increasing radius, and this is true for all the streams.

4.4. Stream kinematics

The only aspect of the algorithm we are interested to discuss in more detail at this level is how much (and what kind) of physical information COSTA can provide, besides the stream detection. In fact, despite the detection is important *per se*, as it provides candidates for follow-up observations (e.g. deep imaging, higher resolution spectroscopy), to have some predictions about relevant intrinsic properties, e.g. surface brightness, a trustworthy estimate of the velocity dispersion and, possibly, the membership of particles, is fundamental to plan such follow-up programs.

As introduced in §4.3, the estimation of the true kinematics of the stream is equivalent to estimate what is the real number of true particles belonging to the stream and the fraction of contaminants from the background system as a function of the set-ups. In principle, one can think that this should depend on the structure of the stream: compact, well populated and very cold streams should produce almost no contaminants, while very diffuse warmer streams would easier be contaminated by particles of the galaxy halo, having similar velocities to that of the central galaxy. However, as we will discuss in the next §4.5, contaminants do not have a huge effect on the estimation of the velocity dispersion of the stream, since by construction COSTA picks up particles with similar velocity.

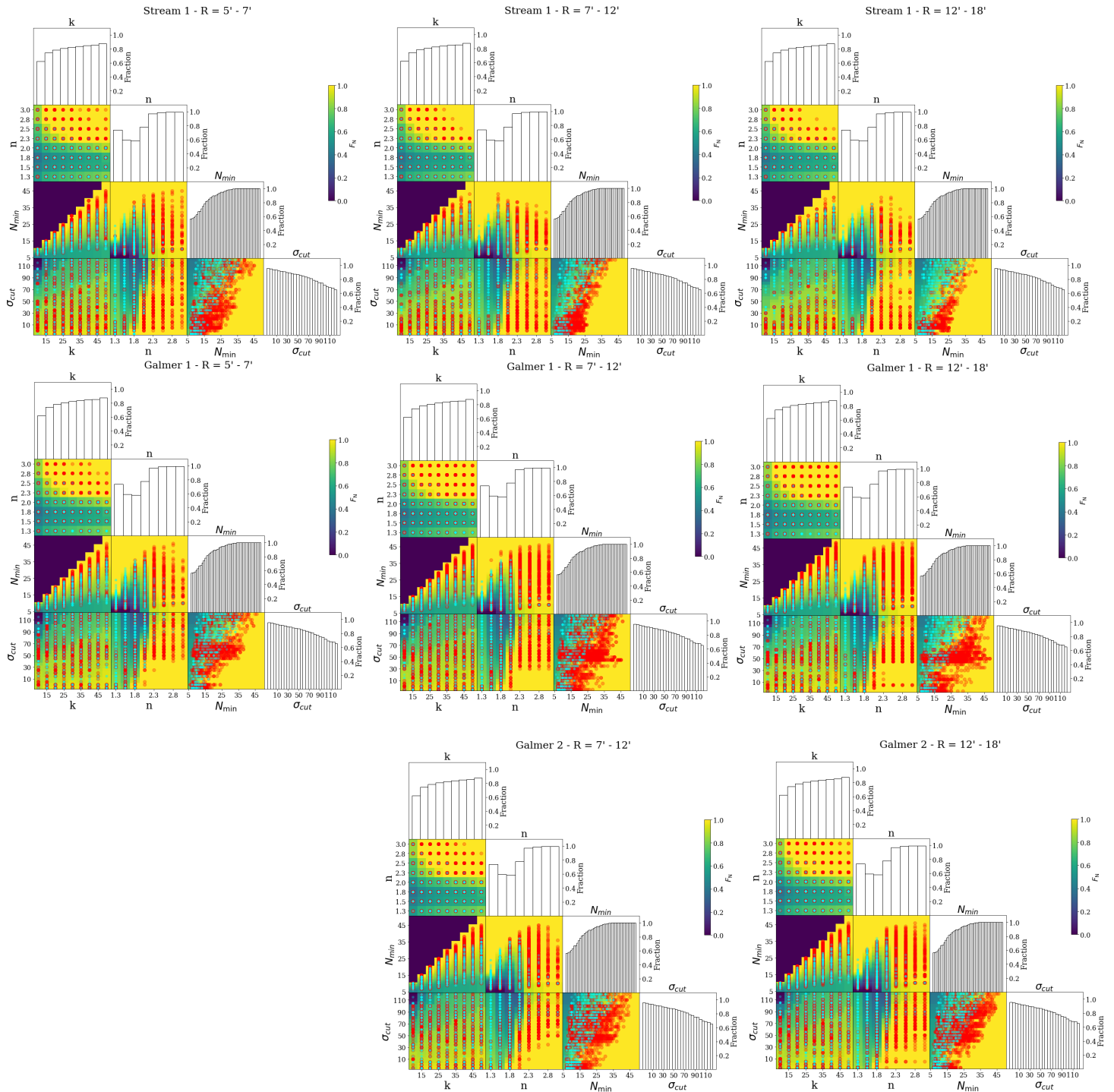


Fig. 11. Stream (red points) and spurious structures (cyan points) overlapped on the Fornax cluster reliability maps in the different shells (left column $R = 5' - 7'$, middle columns $R = 7' - 12'$, right column $R = 12' - 18'$) and for the three different simulated streams (top: *stream 1*, middle: *galmer1* and bottom *galmer2*).

In Fig. 12 we show the density plot of the recovered streams in the $N_{\min} - \sigma$ diagram, cleaned by using a threshold of $F_N = 0.5$ in the $n - N_{\min}$ panel, in the $R = 7' - 12'$ shell, as indicative of the ability to recover the stream kinematics. The results for the other two annuli are similar to these obtained for the central one. We notice that, differently from the Galmer simulations, we construct the streams with a given velocity dispersion, and thus we can check if the 'real value' is recovered. From the figure, it is evident that the set-ups where the stream is detected ac-

cumulate around the true velocity dispersion of the streams (35 km s⁻¹, 45 km s⁻¹, 62 km s⁻¹ for *stream 1*, *galmer 1* and *galmer 2*, respectively), indicated by the dashed black line. In particular, the median of the σ_{mea} distribution is found to be 16 ± 24 , 52 ± 15 , 62 ± 28 , i.e. consistent within 1σ uncertainties.

We notice that the difference between the median values and the true velocity dispersion values are of the same order of magnitudes than normal measurement errors for mid-resolution spectroscopy. For *stream 1*, however, the mean value is below the

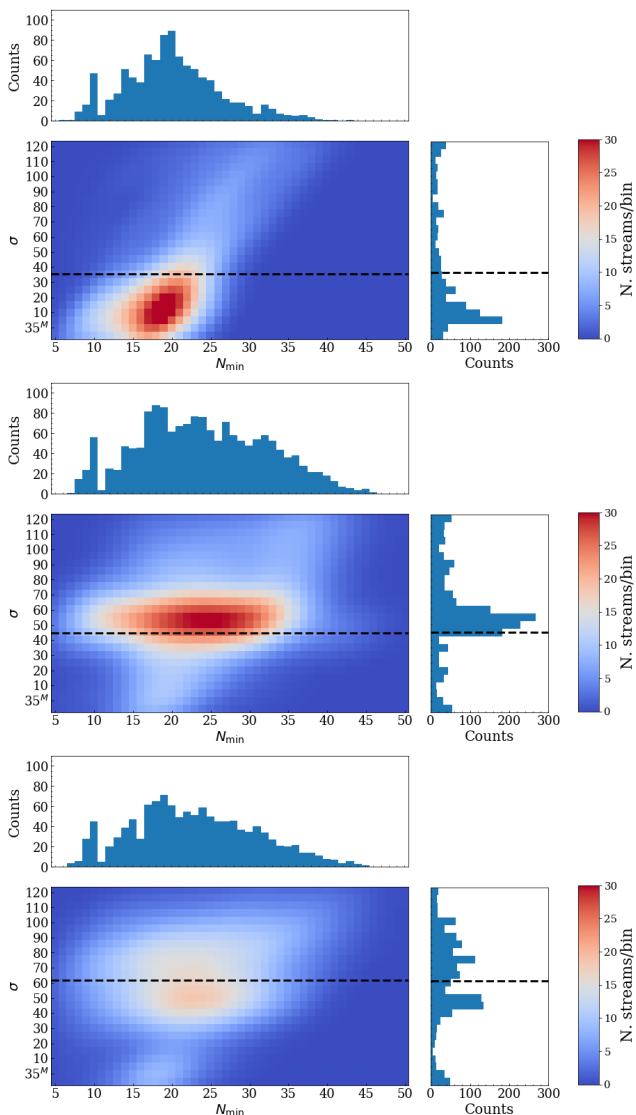


Fig. 12. Density plot in the $N_{\min} - \sigma$ diagram, and number counts of the recovered artificial streams for the middleshell (i.e. 7'-12') for *stream 1* (top), *galmer 1* (middle) and *galmer 2* (bottom). The horizontal dashed line show the true velocity dispersion of each stream. The sample has been cleaned by using $\text{Frac} = 0.5$ as threshold in the $n - N_{\min}$ space. Data have been smoothed with a Gaussian kernel having a bandwidth equal to 3.

accuracy allowed by the velocity, hence the median value just reveals that the assumed precision does not allow to recover the true kinematics, for which a higher velocity accuracy is required.

We also estimate the median number of particles recovered for each stream, to check whether COSTA allows us to infer the total “luminosity” associated to the stream, and find a median of $N_{\text{recov}} = 22, 31, 29$ for *stream 1*, *galmer 1* and *galmer 2*, respectively. These median values are very similar to the true number of particles belonging to the stream (20, 30, 30, see Tab. 5), even if we expect that not all of these particles are truly belonging to the stream (see discussion in the next session).

4.5. Contaminants and fraction of recovered particles

We evaluate here the fraction of contaminant (CF, defined in §3.4.2) particles within the different streams as a function of the

different parameters. We use the Fornax simulations to figure how the contamination can change depending on stream compactness (from the compact *stream 1*, to the very diffuse *galmer 2*), internal velocity dispersion and position within the central potential. We stress that this is a test that one can do only a posteriori, by placing stream candidates in the Montecarlo simulations at the right distance and with the right geometry to perform a “contamination run”. Nevertheless this is useful in order to assess what is the realistic contamination for a given stream.

Our main goal is to provide a general example to show the impact of contaminants on the inference one can derive from COSTA candidates on the intrinsic properties of the streams.

We show in Fig. 13 the trend of CF as a function of the different set-up parameters, for every shell for the three streams. We see a clear dependence of the CF on N_{\min} and on k : i.e. the larger N_{\min} and k are, the higher the number of contaminants is. This is valid for all the streams, in all the shell, but the slope of *stream 1* is steeper and reaches larger CF, especially for N_{\min} . A similar trend is also present for the velocity dispersion cut-off, although it is more noisy and dependent on the shell one considers (more evident at lower radii. For n , instead, the CF is constant around $\text{CF} \sim 0.2 - 0.3$.

In the worst cases we see an increase up to 60% for *stream 1* and $\sim 40\%$ for the two *galmer* streams, for $\sigma_{\text{cut}} > 100 \text{ km s}^{-1}$ and $N_{\min} > 35$. The main reason for the larger contamination is that, while the number of recovered true particles remain almost constant, the larger σ_{cut} and N_{\min} make COSTA select more particles with compatible velocities, but not belonging to the stream. For $k = 50$, the CF reaches the highest level of 50% for the inner radial bin, while it stays below 40% for the outer ones. For any value of n , the CF is always below 40% and, also in this case, it is on average lower for the outer bins with respect to the inner one.

The number of particles recovered has a strong dependence on the number of k (neighbors), as we can expect, and it also has a small dependence on the value n of the sigma clipping: higher values of n give better results. Completeness and contaminant fraction are very similar in the case of the two *galmer* streams, even if they have different sizes. This suggests us that COSTA is able to recover even diffuse streams, e.g. the frequency of the recovering is independent of the dimension of the structure; although we speculate that it could be harder to detect these kind of streams in the denser region, where the noise due to the hot component of the cluster increases.

It is also instructive to verify the correlation between the number of the recovered particles and the set-up parameters. To do that, we define the true completeness (TC) as

$$\text{TC} = \frac{\# \text{ recovered stream particles}}{\# \text{ true stream particles}}$$

where the true stream particle numbers are given in Table 5 for the three simulated streams. The TC is used here to figure what is the range of parameter set-ups that maximize the number of recovered particles over the real ones, by contemporary implying a low CF.

All quantities listed above are not known in observations and depend on the specific data-set and on the distance (i.e. the local particle density). To investigate the effect of distance, we plot, the values of the TC (transparent triangles) parameter and of the OC (full dots) parameter, defined in §3.4.2, for the three simulated streams in the three different shells.

The TC has overall an increasing trend with increasing values of all the set-up parameters. This indicates that COSTA recovers

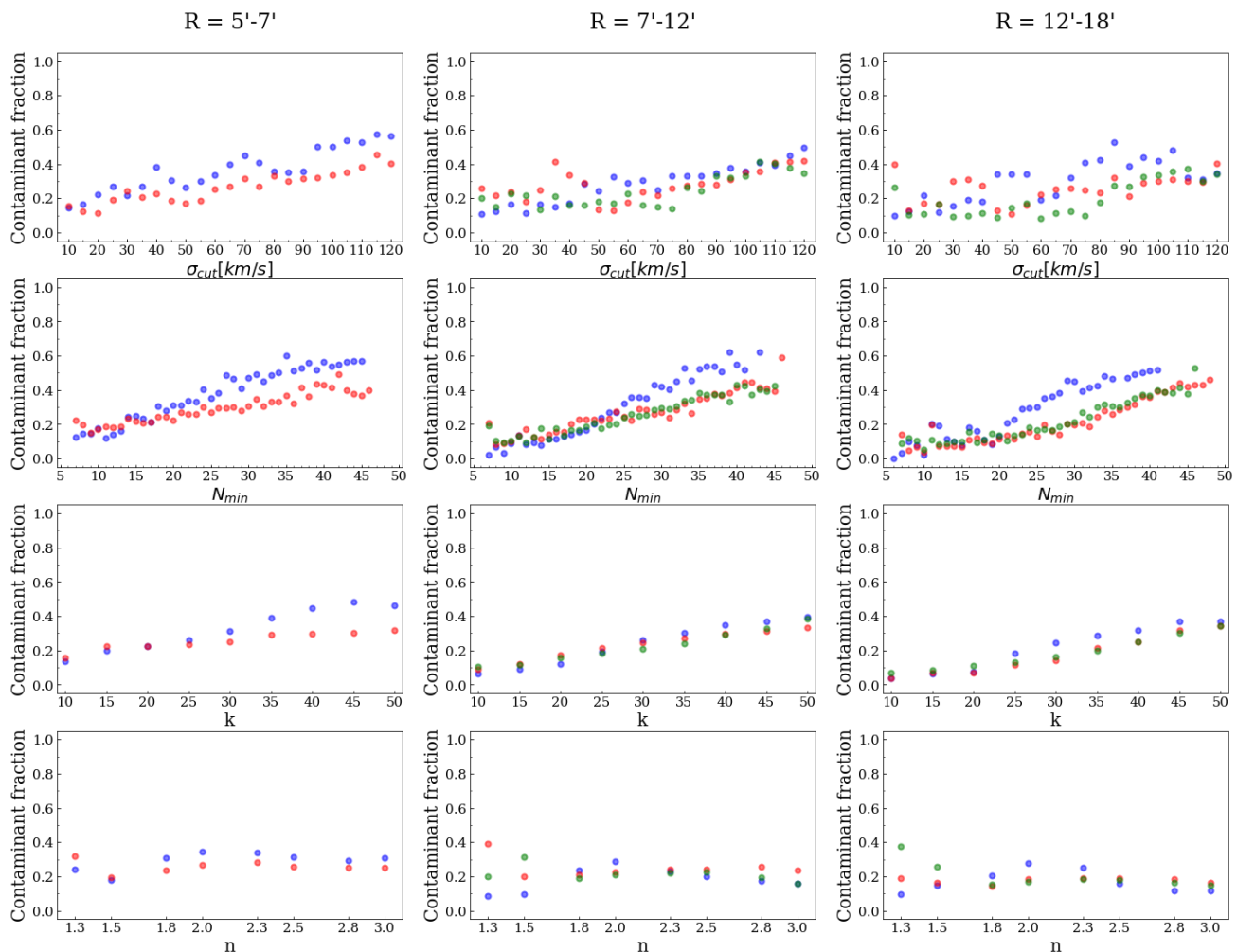


Fig. 13. Contaminant Fraction as a function of the set-up parameters for the $R = 5' - 7'$ shell (left column), the $R = 7' - 12'$ shell (middle column) and the $R = 12' - 18'$ shell (right column). Red points are for the *galmer 1* stream, green points for the *galmer 2* stream and blue points for *stream 1*.

more particles by using stronger constraints (i.e. larger number of neighbors, larger number of particles). However, this also causes a larger number of contaminants, as seen in Fig. 13. We also note that the behavior of the TC is more 'extreme' in the case of the *galmer* streams (red and green points). We speculate that this can be due to the fact that *stream 1* is much more compact than the other two.

The observed completeness (full dots) instead, decreases for larger σ_{cut} , N_{min} and k while it stays roughly constant.

A compromise rule-of-thumb we can derive cross-checking Fig. 12, Fig. 13 and Fig. 14 is that if a stream is found with different set-ups with similar reliability, one should first of all select the parameters that better reproduce its kinematics: the median of the distributions shown in Fig. 12 for N_{min} and σ_{cut} . Then, one should try to select values for n and k for which the OB and TC are similar, while the CF is the minimum possible. For the streams simulated here, this region is around the following values: $k \sim 25 - 30$ and $n \geq 1.8$. This should allow for a reasonable completeness ($\sim 80\%$), with a contamination that is $\sim 50\%$ in the worst case (i.e. high σ_{cut}), or lower than that. It is important to stress, however, that these numbers depends on the system one considers and on the morpho-kinematic characteristics of the streams one aims at recovering. Thus, each run

of COSTA needs to be properly trained with ad-hoc Montecarlo simulations before the algorithm can be used with real data.

Finally, we check how accurate COSTA can reconstruct the intrinsic properties of the streams. The presence of contaminants (estimated to be of the order of 20% of the total number of particles, for low σ_{cut} , if the rule-of-thumb holds) is expected to alter the properties of the recovered stream. In fact, these should have a hotter kinematics and be characterized by a higher velocity dispersion. However, to be selected as friend-of-friend particles, they likely have velocities reasonably compatible with the bulk of the stream, so the effect should not be dramatic. From Fig. 12, we see that the smaller the cut-off is, the smaller the measured stream dispersion is, although, if the adopted cut-off is larger than the real stream dispersion, the dispersion estimates tend to saturate around the true dispersion value. This implies that, if on one hand, using a too large cut-off does not produce a dramatic overestimate of the true velocity dispersion, on the other hand too small cut-offs might produce an underestimation of the stream velocity dispersion. Thus, adopting a larger cut-off would be the safest choice, to have a more realistic estimate of the stream dispersion, but, as discussed before, this is at the cost of a larger fraction of contaminants.

Overall, both the number of particles of the stream and the stream velocity dispersion are underestimated by COSTA. These

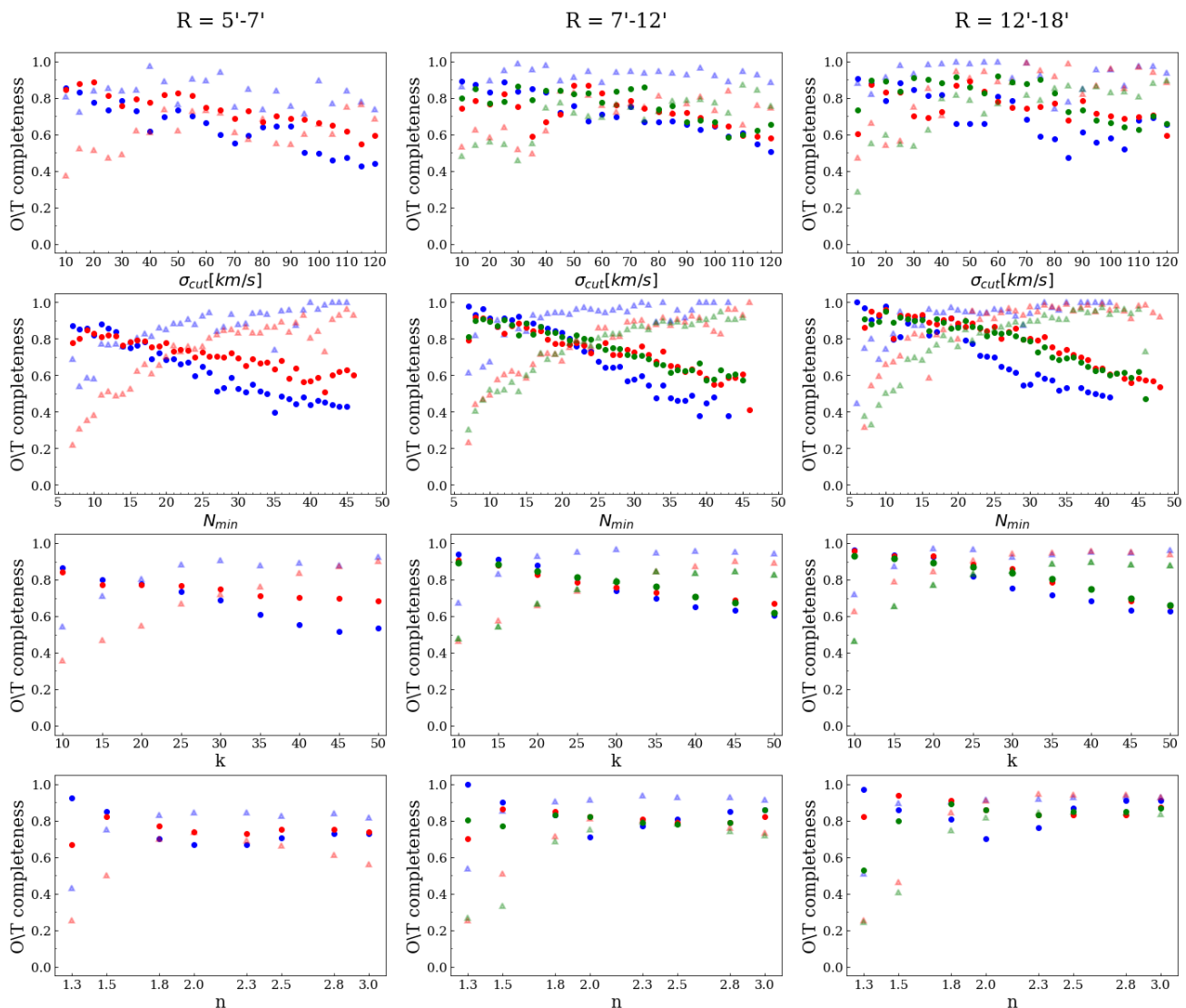


Fig. 14. Observed completeness (full dots) and True completeness (transparent triangles) as a function of the set-up parameters for the $R = 5' - 7'$ shell (left column), the $R = 7' - 12'$ shell (middle column) and the $R = 12' - 18'$ shell (right column). The color code is the same as in Fig. 13: red points for *galmer 1*, green points for *galmer 2* and blue points for *stream 1*.

two quantities are the major parameters we want to retrieve for our stream candidates, because they can give information about the amount of dispersed stellar mass per event and the dispersion of the parent dwarf galaxy, and likely its virial mass. However, the optimization of the set-up to recover the best estimates is beyond the current goals of the preliminary test carried on in this paper, as we are primarily interested in the detection of the streams.

In conclusion, for what we have discussed in this section we are confident that COSTA is able to find real streams in our data, if any.

5. Conclusion

In this work we have introduced COSTA (COLD SStream finder Algorithm): a new tool for the detection of cold kinematics substructures in the outer halo of massive galaxies, as probe of their recent and past merger history.

As all massive galaxies built their halo through minor mergers (e.g. Amorisco 2019), it is of enormous value to reveal such tidal debris and infer their intrinsic properties in order to unveil

the mechanisms playing a role in the mass assembly history of massive galaxies.

Since these structures have a very low surface brightness, it is incredibly difficult to detect them by means of photometric observations alone. In the last years, thanks to new instrumentation that allowed for more accurate spectroscopy, the research of merger signatures shifted to the exploration of the phase-space of kinematical tracers. So far, supported also by numerical simulations and analytical models, the detection of streams has been limited to the search for shells and narrow diagonal tracks, having a chevron-like shape in the position-velocity diagram (e.g. Romanowsky et al. 2012; Longobardi et al. 2015). Unfortunately, these patterns are not produced by low dispersion streams made of a handful of particles (of the order of few tens) and originated from dwarf galaxies in a recent encounter with a massive galaxy (see e.g. Fig. 4). COSTA allows us to search for this low surface brightness streams in a *systematic way* in the phase-space, being able to detect cold kinematics substructures moving in a warm/hot environment composed by relaxed particles.

COSTA relies on a deep friend-of-friend algorithm that, through an iterative sigma clipping, detaches groups of neighbors particles with a cold kinematics (with velocity dispersion of the order of tens of km s^{-1}).

The algorithm has four free parameters that have to be set with Montecarlo simulations, mimicking the real system under exam.

The final aim of this work has been the detection of streams with COSTA in simulated systems, and we are fully confident that our algorithm is able to detect them in real cases too, if any. In particular, in this work, we have

- discussed the ability of COSTA in recovering cold substructures in different dynamical conditions, from cold giant spiral galaxies to giant ellipticals living in the core of large cluster of galaxies (sections §3 and §4). The general results is that, COSTA is able to detect real substructures with a variety of combinations of the four free parameters and with a limited number of spurious events, if one selects the regions in the parameter space that maximize the reliability of a stream detection and minimize the chance of false positive.
- shown that the COSTA algorithm works in finding cold streams embedded in an hotter environment. The efficiency of COSTA in recovery streams heavily depends on the ratio between the velocity dispersion of the stream and that of the host galaxy, favoring cold streams embedded in a hot surrounding. In fact, the performance of COSTA are much worse when the difference between the velocity dispersion of the giant and that of the dwarf intruder is very small (see the case of a gSa-dSa interaction, §3.5, versus the case of a gE0-dE0, §3.4, and that of the Fornax Core, §4). The algorithm also slightly depends on the number of tracers of the stream (i.e. the mass ratio of the dwarf and the giant galaxy, see §4).
- shown that the difference between the measured and the real velocity dispersion is similar to the uncertainties on velocities, hence the assessment of the stream kinematics would improve if higher spectroscopic resolution is available (section §3.4.4).
- demonstrated that in order to best estimate the reliability of the COSTA set-ups, we have first to construct a realistic realization in the phase space of the system under analysis. This is not an easy task and it also needs customized Montecarlo realizations (section §4). Furthermore, the reliability map one can derive might depend on how accurate is the description of the underlying “relaxed” system with respect to the stream population. However, we note that an over-detailed dynamical description of a given system, can also incorporate substructures as a part of the relaxed component, hence reducing the chance to be recognized as a true substructure. We believe that the Montecarlo approach, as in §4, is a reasonable start, but we cannot exclude that more sophisticated relaxed model based on N-body codes will be used in the future to refine the predictions on real systems applying COSTA to real data.
- derived a rule-of-thumb to unveil the real kinematics of a given stream, and hence to get insights on the properties of the parent galaxy from which these particles have been stripped. We note however that, overall, COSTA underestimates the true velocity dispersion of the stream (S5).

To conclude, we have proved here that COSTA is a useful tool to detect stream candidates originated by close galaxy encounters in a 3D phase space, e.g. using right ascension, declination and radial velocity of particles as input. Since its ability increases when the stream is considerably colder than the

surrounding environment, its natural implementation shall be galaxy clusters, where the high velocity dispersion of the relaxed particles moving in the potential well of the cluster makes it easier to unveil a group of particles coherent both in position and in velocity. Nevertheless, we demonstrated that COSTA is also suitable to other situations like galaxy-galaxy encounters hence, in principle, it could be used everywhere a sample of kinematic tracers is available.

Acknowledgements. NRN acknowledges financial support from the "One hundred top talent program of Sun Yat-Sen University" grant N. 71000-18841229, and from the European Union Horizon 2020 research and innovation programme under the Marie Skłodowska-Curie grant agreement n. 721463 to the SUNDIAL ITN network. MG acknowledges support from the INAF fund "Funzionamento VST" (1.05.03.02.04). CS is supported by a Hintze Fellowship at the Oxford Centre for Astrophysical Surveys, which is funded through generous support from the Hintze Family Charitable Foundation.

References

- Amorisco, N. C. 2019, MNRAS, 482, 2978
- Arnaboldi, M., Gerhard, O., Aguerri, J. A. L., et al. 2004, The astrophysical journal, Letters, 614, L33
- Arnaboldi, M., Ventimiglia, G., Iodice, E., Gerhard, O., & Coccato, L. 2012, Astronomy and Astrophysics, 545, A37
- Barnes, J. & Hut, P. 1986, Nature, 324, 446
- Bate, N. F., Conn, A. R., McMonigal, B., et al. 2014, MNRAS, 437, 3362
- Belokurov, V. & Koposov, S. E. 2016, MNRAS, 456, 602
- Belokurov, V., Zucker, D. B., Evans, N. W., et al. 2006, ApJ, 642, L137
- Bullock, J. S. & Johnston, K. V. 2005, ApJ, 635, 931
- Chilingarian, I. V., Di Matteo, P., Combes, F., Melchior, A.-L., & Semelin, B. 2010, Astronomy and Astrophysics, 518, A61
- Coccato, L., Arnaboldi, M., & Gerhard, O. 2013, Monthly Notices of the RAS, 436, 1322
- Coccato, L., Gerhard, O., Arnaboldi, M., et al. 2009, Monthly Notices of the RAS, 394, 1249
- Cooper, A., Cole, S., Frenk, C., et al. 2010, Monthly notices of the royal astronomical society, 406, 744
- Cooper, A. P., Martínez-Delgado, D., Helly, J., et al. 2011, ApJ, 743, L21
- Cortesi, A., Merrifield, M. R., Arnaboldi, M., et al. 2011, MNRAS, 414, 642
- Corwin, H. G., de Vaucouleurs, A., & de Vaucouleurs, G. 1985, Southern galaxy catalogue. A catalogue of 5481 galaxies south of declination -17 grad. found on 1.2m UK Schmidt IIIa J plates
- Côté, P., McLaughlin, D. E., Cohen, J. G., & Blakeslee, J. P. 2003, The astrophysical journal, 591, 850
- D’Abrusco, R., Cantiello, M., Paolillo, M., et al. 2016, Astrophysical Journal, Letters, 819, L31
- De Lorenzi, F., Gerhard, O., Coccato, L., et al. 2009, Monthly Notices of the RAS, 395, 76
- De Lucia, G. & Blaizot, J. 2007, MNRAS, 375, 2
- Douglas, N. G., Napolitano, N. R., Romanowsky, A. J., et al. 2007, The astrophysical journal, 664, 257
- Durrell, P. R., Mihos, J. C., Feldmeier, J. J., Jacoby, G. H., & Ciardullo, R. 2003, ApJ, 582, 170
- Faber, S. M. & Jackson, R. E. 1976, ApJ, 204, 668
- Fahion, K., Lyubenova, M., Hilker, M., et al. 2020, A&A, 637, A26
- Feldmeier, J. J., Ciardullo, R., Jacoby, G. H., & Durrell, P. R. 2004, ApJ, 615, 196
- Forbes, D. A., Spitler, L. R., Strader, J., et al. 2011, Monthly Notices of the RAS, 413, 2943
- Foster, C., Lux, H., Romanowsky, A. J., et al. 2014, Monthly Notices of the RAS, 442, 3544
- Gallagher, III, J. & Ostriker, J. 1972, The astrophysical journal, 77, 288
- Gilbert, A. M. & Vacca, W. D. 2009, Astrophysics and Space Science, 324, 147
- Gingold, R. A. & Monaghan, J. J. 1982, Journal of Computational Physics, 46, 429
- Gregg, Michael D.; West, M. J. 1998, Nature, 396
- Hartke, J., Arnaboldi, M., Longobardi, A., et al. 2017, in IAU Symposium, Vol. 323, Planetary Nebulae: Multi-Wavelength Probes of Stellar and Galactic Evolution, ed. X. Liu, L. Stanghellini, & A. Karakas, 293–297
- Helmi, A., White, S. D. M., de Zeeuw, P. T., & Zhao, H. 1999, Nature, 402

- Hendel, D., Johnston, K. V., Patra, R. K., & Sen, B. 2019, *MNRAS*, 486, 3604
- Henriksen, L. 1990, *The astrophysical journal*, 356, 359
- Hui, X., Ford, H. C., Freeman, K. C., & Dopita, M. A. 1995, *The astrophysical journal*, 449, 592
- Ibata, R., Irwin, M., Lewis, G., Ferguson, A. M. N., & Tanvir, N. 2001a, *Nature*, 412, 49
- Ibata, R., Irwin, M., Lewis, G. F., & Stolte, A. 2001b, *ApJ*, 547, L133
- Ibata, R., Irwin, M., Lewis, G. F., & Stolte, A. 2001c, *Astrophysical Journal Letters*, 547, L133
- Ibata, R., Lewis, G. F., Irwin, M., Totten, E., & Quinn, T. 2001d, *The astrophysical journal*, 551, 294
- Ibata, R. A., Gilmore, G., & Irwin, M. J. 1994, *Nature*, 370, 194
- Ibata, R. A., Gilmore, G., & Irwin, M. J. 1995, *MNRAS*, 277, 781
- Ibata, R. A., Wyse, R. F. G., Gilmore, G., Irwin, M. J., & Suntzeff, N. B. 1997, *Astronomical Journal*, 113, 634
- Iodice, E., Spavone, M., Cantiello, M., et al. 2017, *The Astrophysical Journal*, 851
- Iodice, E.; Capaccioli, M., Grado, A., Limatola, L., et al. 2016, *The Astrophysical Journal*, 820
- Johnston, K. V., Bullock, J. S., Sharma, S., et al. 2008, *ApJ*, 689, 936
- Kado-Fong, E., Greene, J. E., Hendel, D., et al. 2018, *ApJ*, 866, 103
- Koch, A., Rich, R. M., Reitzel, D. B., et al. 2008, *The astrophysical journal*, 689, 958
- Kourkchi, E., Khosroshahi, H. G., Carter, D., et al. 2012, *MNRAS*, 420, 2819
- Liu, F. S., Lei, F. J., Meng, X. M., & Jiang, D. F. 2015, *MNRAS*, 447, 1491
- Longobardi, A., Arnaboldi, M., & Gerhard, O. 2015, *Galaxies*, 3, 212
- Longobardi, A., Arnaboldi, M., Gerhard, O., Pulsoni, C., & Söldner-Rembold, I. 2018, *A&A*, 620, A111
- Lucy, L. B. 1977, *AJ*, 82, 1013
- Majewski, S. R., Skrutskie, M. F., Weinberg, M. D., & Ostheimer, J. C. 2003, *The astrophysical journal*, 599, 1082
- Malhan, K. & Ibata, R. A. 2018, *MNRAS*, 477, 4063
- Malumuth, E. & Richstone, D. 1984, *The astrophysical journal*, 276, 413
- Martínez-Delgado, D., Gabany, R. J., Crawford, K., et al. 2010, *AJ*, 140, 962
- McConnachie, A. W., Irwin, M. J., Ibata, R. A., et al. 2009, *Nature*, 461, 66
- Merrett, H. R., Kuijken, K., Merrifield, M. R., et al. 2003, *MNRAS*, 346, L62
- Merrett, H. R., Merrifield, M. R., Douglas, N. G., et al. 2006, *MNRAS*, 369, 120
- Merritt, D. 1985, *The astrophysical journal*, 289, 18
- Mihos, J. C., Harding, P., Feldmeier, J., & Morrison, H. 2005, *ApJ*, 631, L41
- Mihos, J. C., Harding, P., Feldmeier, J. J., et al. 2017, *ApJ*, 834, 16
- Moore, B., Katz, N., Lake, G., Dressler, A., & Oemler, A. 1996, *Nature*, 379
- Mouhcine, M., Ibata, R., & Rejkuba, M. 2011, *MNRAS*, 415, 993
- Naab, T., Johansson, P. H., & Ostriker, J. P. 2009, *ApJ*, 699, L178
- Naab, T., Johansson, P. H., Ostriker, J. P., & Efstathiou, G. 2007, *ApJ*, 658, 710
- Napolitano, N. R., Arnaboldi, M., & Capaccioli, M. 2002, *Astronomy and Astrophysics*, 383, 791
- Napolitano, N. R., Arnaboldi, M., Freeman, K. C., & Capaccioli, M. 2001, *Astronomy and Astrophysics*, 377, 784
- Napolitano, N. R., Pannella, M., Arnaboldi, M., et al. 2003, *The Astrophysical Journal*, 594
- Napolitano, N. R., Romanowsky, A. J., Capaccioli, M., et al. 2011, *MNRAS*, 411, 2035
- Napolitano, N. R., Romanowsky, A. J., Coccato, L., et al. 2009, *Monthly Notices of the RAS*, 393, 329
- Navarro, J. F., Frenk, C. S., & White, S. D. M. 1997, *ApJ*, 490, 493
- Nipoti, C. 2017, *MNRAS*, 467, 661
- Oser, L., Naab, T., Ostriker, J. P., & Johansson, P. H. 2012, *ApJ*, 744, 63
- Oser, L., Ostriker, J. P., Naab, T., Johansson, P. H., & Burkert, A. 2010, *ApJ*, 725, 2312
- Ostriker, J. & Tremaine, S. 1975, *The astrophysical journal*, 202, L113
- Peng, E. W., Ford, H. C., & Freeman, K. C. 2004, *arXiv e-prints*, astro
- Pota, V., Forbes, D. A., Romanowsky, A. J., et al. 2013, *Monthly Notices of the Royal Astronomical Society*, 428
- Pota, V., Napolitano, N. R., Hilker, M., et al. 2018, *Monthly Notices of the RAS*, 481, 1744
- Read, J. I., Wilkinson, M. I., Evans, N. W., Gilmore, G., & Kleyna, J. T. 2006, *Monthly Notices of the Royal Astronomical Society*, 366
- Richtler, T., Salinas, R., Misgeld, I., et al. 2011, *A&A*, 531, A119
- Romanowsky, A. J., Brodie, J. P., Bullock, J. S., et al. 2009, in *ArXiv Astrophysics e-prints*, Vol. 2010, astro2010: The Astronomy and Astrophysics Decadal Survey
- Romanowsky, A. J., Douglas, N. G., Arnaboldi, M., et al. 2003, *Science*, 301, 1696
- Romanowsky, A. J., Strader, J., Brodie, J. P., et al. 2012, *The astrophysical journal*, 748, 29
- Ruszkowski, M. & Springel, V. 2009, *ApJ*, 696, 1094
- Schuberth, Y., Richtler, T., Hilker, M., et al. 2010, *Astronomy and Astrophysics*, 513, A52
- Sheardown, A., Roediger, E., Su, Y., et al. 2018, *The astrophysical journal*, 865, 118
- Shih, H.-Y. & Méndez, R. H. 2010, *ApJ*, 725, L97
- Spiniello, C., Napolitano, N. R., Arnaboldi, M., et al. 2018, *Monthly Notices of the RAS*, 477, 1880
- Starkenburger, E., Helmi, A., Morrison, H. L., et al. 2009, *The astrophysical journal*, 698, 567
- Tal, T., van Dokkum, P. G., Nelan, J., & Bezanson, R. 2009, *AJ*, 138, 1417
- Veljanoski, J. & Helmi, A. 2016, *Astronomy and Astrophysics*, 592, A55
- Weinzirl, T., Jogee, S., Neistein, E., et al. 2014, *MNRAS*, 441, 3083
- White, S. D. M. 1976, *Monthly Notices of the Royal Astronomical Society*, 177
- White, S. D. M. & Rees, M. J. 1978, *MNRAS*, 183, 341
- Willman, B., Governato, F., Wadsley, J., & Quinn, T. 2004, *Monthly Notices of the Royal Astronomical Society*, 355
- Woodley, K. A. & Harris, W. E. 2011, *Astronomical journal*, 141, 27
- Xue, X.-X., Rix, H.-W., Yanny, B., et al. 2011, *ApJ*, 738, 79
- Yanny, B., Newberg, H. J., Kent, S., et al. 2000, *ApJ*, 540, 825